

Recent Study of Nuclear Charge Radii Evolution

Myeong-Hwan Mun, Seonghyun Kim, Eunja Ha, Y. Tanimura

Myung-Ki Cheoun

([Soongsil University](#), [OMEG Institute](#) & [Dept. of Physics](#), Seoul, Korea)

<https://omeg.ssu.ac.kr/>

The 2024 Asian Nuclear Physics Association Symposium

Conference Center, Huizhou-IMP Institute of Modern Physics,
Chinese Academy of Sciences Nov 15–16, 2024 Huizhou City, Guangdong Province,
China

Network calculation for nucleosynthesis

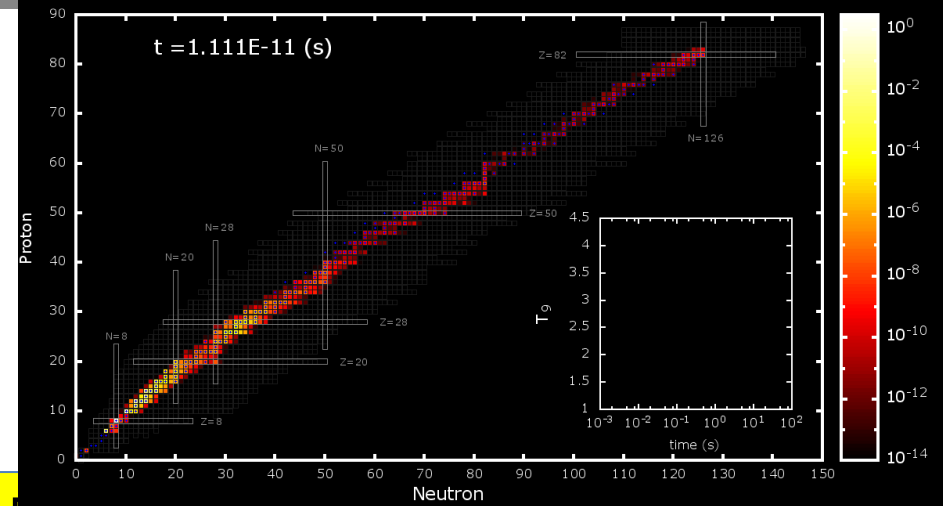
$$\frac{dN_j}{dt} = N_i \lambda_{i,j} - N_j \lambda_{j,h} + \dots \rightarrow \frac{dY_j}{dt} = Y_i \lambda_{i,j} - Y_j \lambda_{j,h} + \dots$$

JINA REALIB

$$Y_j = \frac{N_j}{\rho N_A}$$

+ Modified (n,g) Reactions

+ Neutrino-induced Reactions by QRPA & Branching Ratios



Numerical results for elements abundances

1987 SN model

Pre-supernova Model

Hydrodynamics Model: HCK18, KCK19

★ Modified Neutrino Flux by Self-interaction : w/ and wo/

★ Neutrino Luminosity : EQ and NEQ

Mass Hierarchy : NH and IH

Contents

1. Experimental evidences of OES and Kink structures

1-1. Odd-Even (**Shape**) Staggering (OES) : **Xiaofei Yang Talk (11/15)**

1-2. Kink

2. Deformed Relativistic Hartree Bogoliubov in Continuum (DRHBc) theory and other DFTs

Myeong-Hwan Mun, Seonghyun Kim, Myung-Ki Cheoun, W.Y. So, Soonchul Choi, Phys. Lett.B 847, 138298 (2023)

3. OES and Kink of Hg and Au by DRHBc and other Skyrme DFTs

3-1. OES of Hg and Au

Myeong-Hwan Mun, E. Ha, Y. B. Choi, Myung-Ki Cheoun, PRC 110, 024310 (2024)

3-2. Kink of Hg and Pb

Seonghyun Kim, Myeong-Hwan Mun, Myung-Ki Cheoun and Eunja Ha, PRC 105, 034340 (2022)

4. CM corrections and Magnetic Moments

Y. Tanimura and M. K. Cheoun, PRC 109, 054323 (2024)

5. Summary

LEES2024

Oct. 28 - Nov. 1, 2024

Tohoku University, Sendai, Japan

LOCAL ORGANIZING COMMITTEE

Toshimi SUDA (Chair) *Tohoku*

YUKI HONDA *Tohoku*

Tetsuya OHNISHI *RIKEN*

Kyo TSUKADA *Kyoto*

Shun IIMURA *Rikkyo*

MEETING WEBSITE

<https://indico.lns.tohoku.ac.jp/e/LEES2024>

1. Introduction

SCRIT electron scattering facility

M. Wakasugi et al., NIMB 317 (2013) 668.
T. Ohnishi et al., NIMB 541 (2023) 380.

Requirements for RI beams in SCRIT

Low-energy (\sim keV)

High quality (small emittance)

High intensity ($\sim 10^8$ ions/pulse)

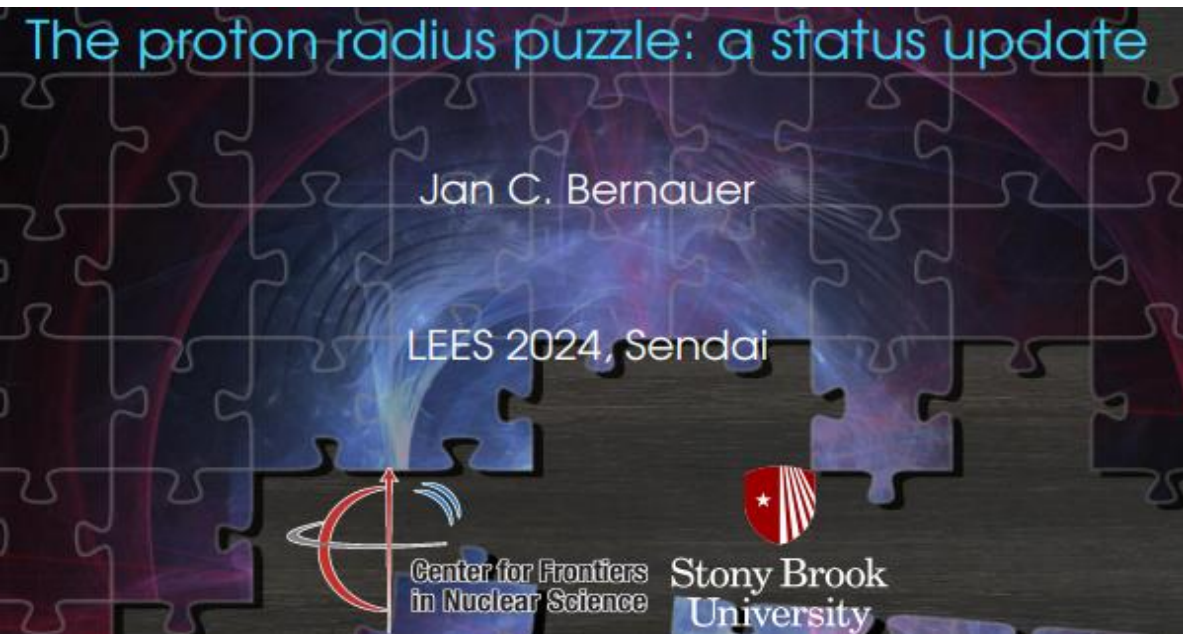
➡ ISOL system: ERIS

Absolute measure of charge radii of RI !!

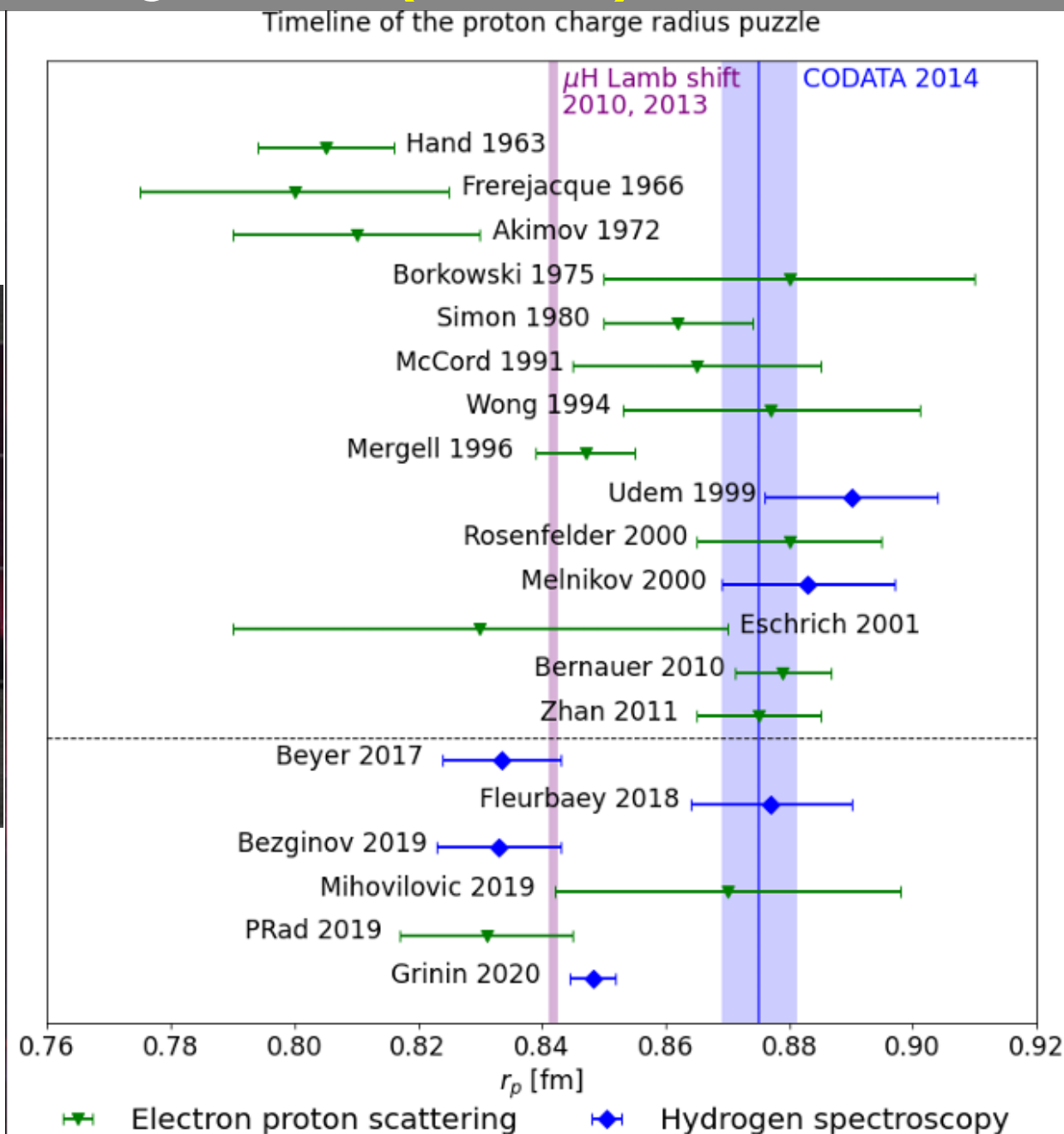
Guangdong, China, Nov. 2024

0. Introduction

Proton Charge Radius (Puzzle ?)



ANPHA Symposium, Huizhou, Guangdong, China, Nov.
15-16, 2024

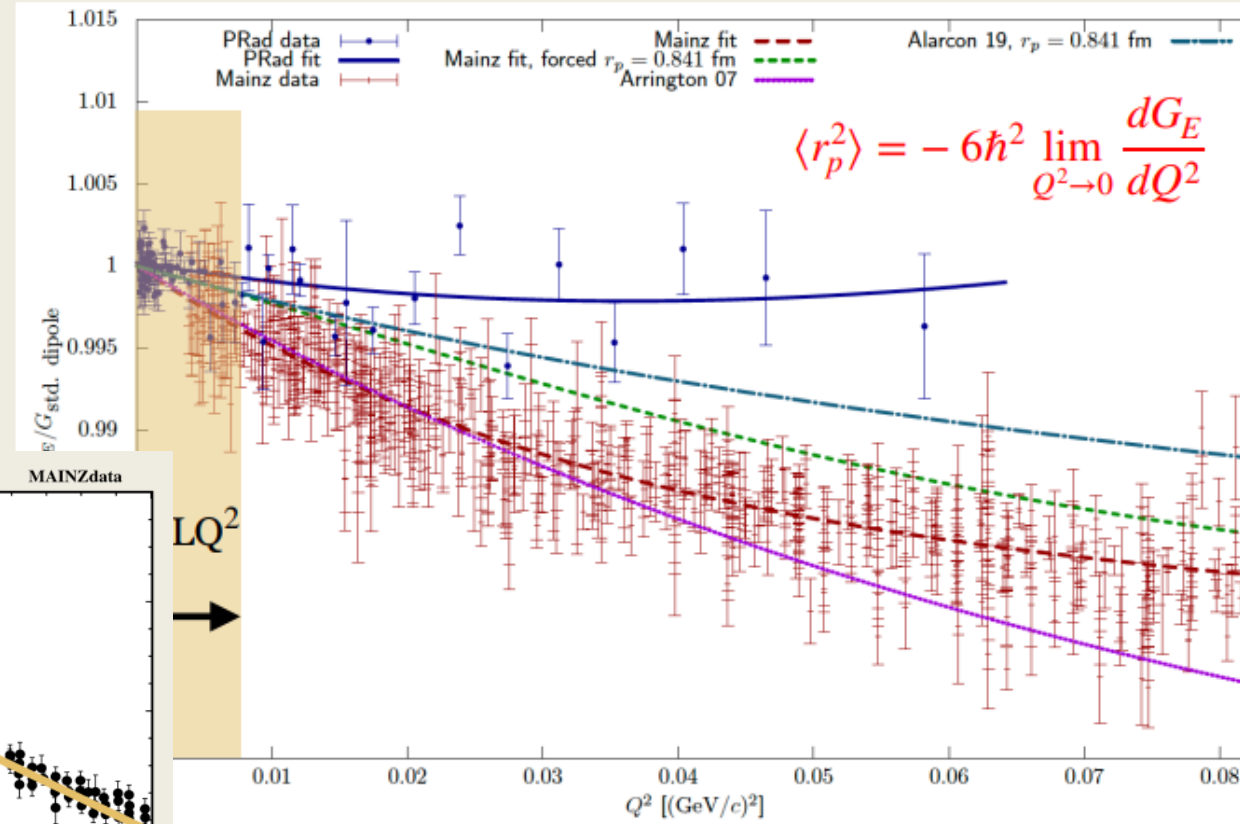


Form factor discrepancy

Electron scattering: Proton electric form factor

$$G_{std}(Q^2) = \frac{1}{\left(1 + \frac{Q^2}{\Lambda^2}\right)^2}$$

with $\Lambda = 0.71 \text{ (GeV/c)}^2$



Different Q^2 -dependencies of the electric form factor

➡ Mainz (2010): $r_p = (0.879 \pm 0.008) \text{ fm}$

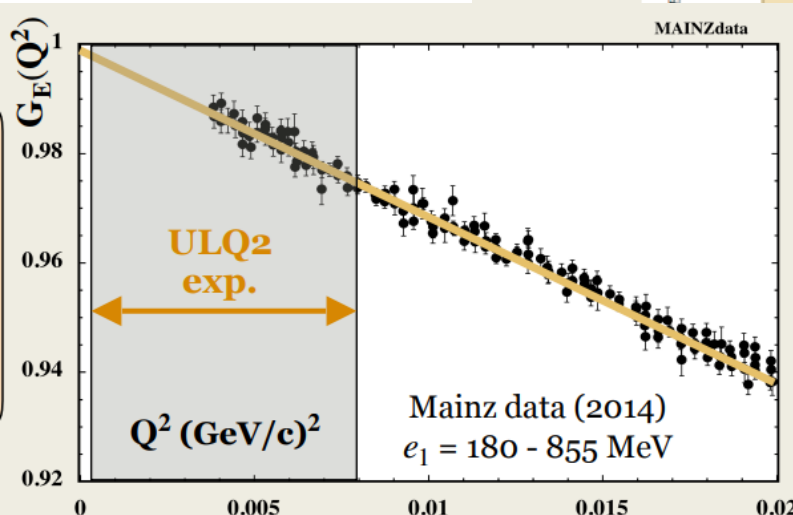
➡ PRad (2019) : $r_p = (0.831 \pm 0.014) \text{ fm}$

3 σ discrepancy!

At least 1 experiment is wrong!

➡ **Need data at low Q^2 : ULQ²!**

➡ **Most reliable measurement!**



Momentum transfer range reached during the ULQ² experiment.

J. C. Bernauer, EPJ Web of Conf. **234**, 01001 (2020)

GPPU seminar

ANPHA Symposium, Huizhou, Guangdong, China, Nov. 15-16, 2024

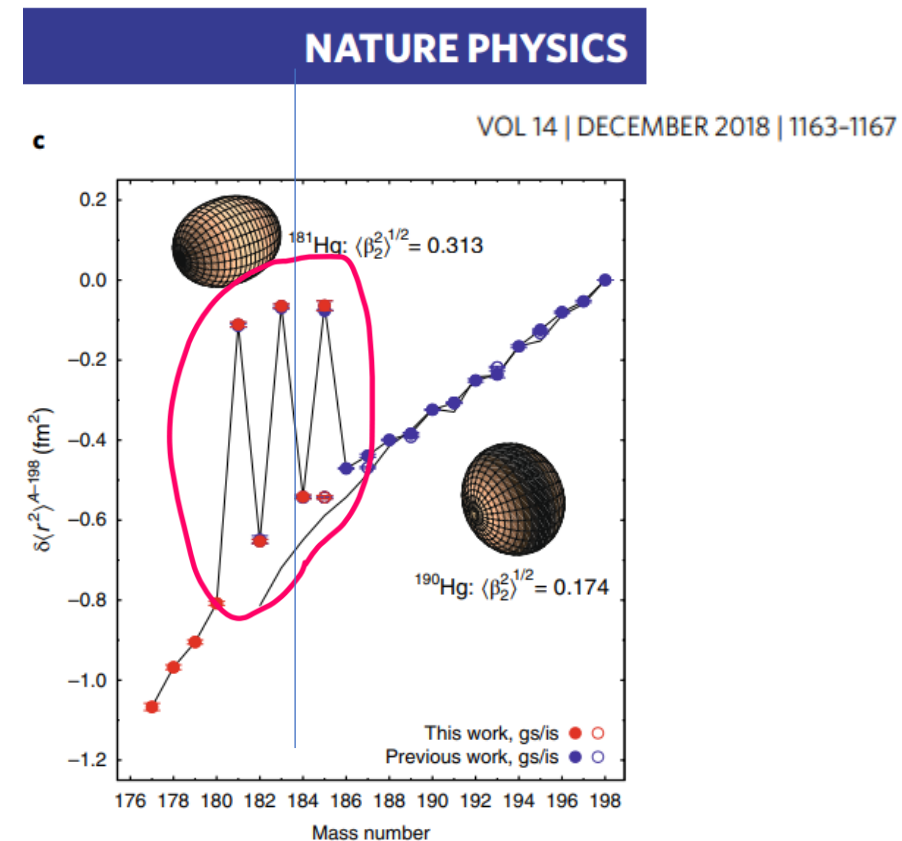


Fig. 1 | An overview of the in-source resonance ionization spectroscopy study of radiogenic mercury isotopes. **a**, Mercury isotopes are produced by proton-induced nuclear reactions in a molten lead target. The vapour effuses into the anode volume of the VADLIS ion source²³, where the atoms are ionized using a three-step resonance photo-ionization scheme (inset). The ions are extracted as a mono-energetic beam at 30 keV. The isotope of interest is selected using the general-purpose mass separator (GPS) and directed towards the most appropriate of the three detection systems shown (see Methods). **b**, By scanning the laser wavelength of the spectroscopic transition (in this case the first step), the isotope shift (IS) and hyperfine structure (HFS) are examined. The isotope shifts are used to calculate the changes in mean-square charge radii $\delta\langle r^2 \rangle$ with respect to $A = N + Z = 198$ along the isotopic chain. **c**, The results of this study appear as filled red circles (ground states, gs) or open red circles (isomeric states, is). ^{177–180}Hg are new measurements, whereas ^{181–185}Hg were re-measured and the data points overlap with those of the literature values (blue circles), as can also be seen by the close agreement between values in Table 1. The error bars correspond to the standard deviation of measurements. Additional scaling uncertainties (not shown) arise from the indeterminacy of the F factor (7%; see ref. ¹⁹) and the specific mass shift, M_{ss} . These are provided in Table 1. The additional continuous black line illustrates the previously measured quasi-spherical trend of the lead nuclei⁶. Sketched insets, representative of the shapes of ¹⁹⁰Hg and ¹⁸¹Hg with a deformation parameter $\langle \beta_2^2 \rangle^{1/2} = 0.174$ and 0.313 respectively, are provided.

Large Shape Staggering in Neutron-Deficient Bi Isotopes

A. Barzakh^{1,*}, A. N. Andreyev,^{2,3} C. Raison,² J. G. Cubiss,² P. Van Duppen,⁴ S. Péru,⁵ S. Hilaire,⁵ S. Goriely,⁶ B. Andel,⁷ S. Antalic,⁷ M. Al Monthery,² J. C. Berengut,⁸ J. Bieroń,⁹ M. L. Bissell,¹⁰ A. Borschevsky,¹¹ K. Chrysalidis,^{12,13} T. E. Cocolios,⁴ T. Day Goodacre,^{14,12,10} J.-P. Dognon,¹⁵ M. Elantkowska,¹⁶ E. Eliav,¹⁷ G. J. Farooq-Smith,^{4,†} D. V. Fedorov,¹ V. N. Fedosseev,¹² L. P. Gaffney,^{18,‡} R. F. Garcia Ruiz,^{10,§} M. Godefroid,¹⁹ C. Granados,^{12,4} R. D. Harding,^{2,12} R. Heinke,^{13,||} M. Huyse,⁴ J. Karls,^{12,20} P. Larmonier,¹² J. G. Li (李冀光),²¹ K. M. Lynch,¹² D. E. Maisson,^{1,22} B. A. Marsh,¹² P. Molkanov,¹ P. Mosat,⁷ A. V. Oleynichenko,^{1,23} V. Panteleev,¹ P. Pykkö,²⁴ M. L. Reitsma,¹¹ K. Rezykina,⁴ R. E. Rossel,¹² S. Rothe,¹² J. Ruczkowski,¹⁶ S. Schiffmann,¹⁹ C. Seiffert,¹² M. D. Seliverstov,¹ S. Sels,^{4,||} L. V. Skripnikov,^{1,22} M. Stryczyk,^{4,25} D. Studer,¹³ M. Verlinde,⁴ S. Wilman,¹⁶ and A. V. Zaitsevskii^{1,23}

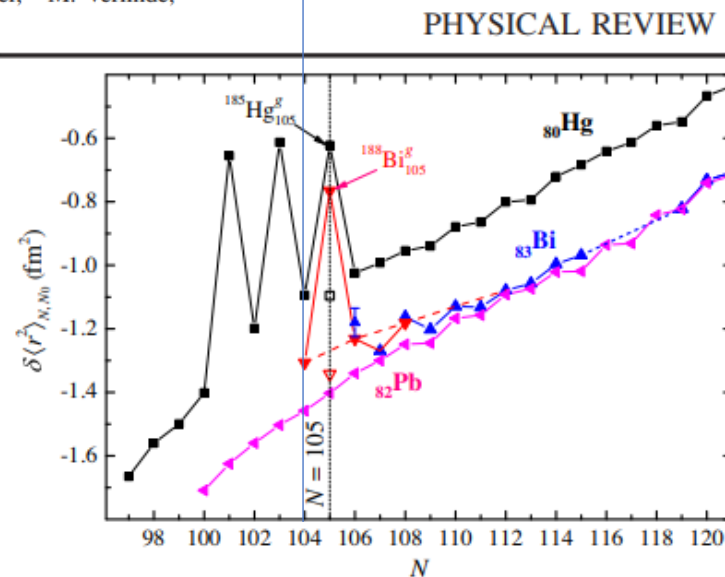


FIG. 2. Changes in the mean-square charge radii for Bi (downward triangles, present work; upward triangles, Refs. [27,55,56]), Pb (leftward triangles, Refs. [5,57,58]), and Hg (squares, Refs. [10–12]) isotopes. Full and hollow symbols label the gs's and isomers, respectively. Data for each chain are shifted along the Y axis to improve visibility. Red dashed line connects the data for the even- N $9/2^-$ Bi gs's to demonstrate deviation from the Pb trend.

PHYSICAL REVIEW LETTERS 127, 192501 (2021)

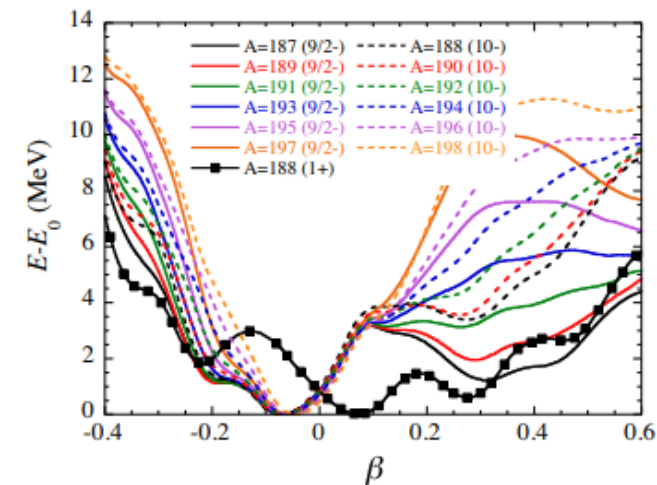


FIG. 3. HFB PESs obtained by blocking the first $9/2^-$ qp in odd- A bismuth isotopes (solid lines), 10^- in even- A ones (dashed lines), and 1^+ in ^{188}Bi (squares). E_0 is the minimal energy of the corresponding PES. For each PES, at least one of the minima has a magnetic moment compatible with experimental data. For $9/2^-$ and 10^- states it is a minimum at $\beta \approx -0.07$, whereas for 1^+ state in ^{188}Bi it is a minimum at $\beta \approx +0.28$.

PHYSICAL REVIEW LETTERS **131**, 202501 (2023)

Editors' Suggestion

Deformation versus Sphericity in the Ground States of the Lightest Gold Isotopes

J. G. Cubiss^{1,*}, A. N. Andreyev,^{1,2} A. E. Barzakh³, P. Van Duppen⁴, S. Hilaire,⁵ S. Péru,⁵ S. Goriely,⁶ M. Al Monthery,¹ N. A. Althubiti,^{7,8} B. Andel⁹, S. Antalic⁹, D. Atanasov,^{10,11} K. Blaum¹⁰, T. E. Cocolios^{7,4}, T. Day Goodacre,^{7,11,†} A. de Roubin,^{10,‡} G. J. Farooq-Smith^{7,4}, D. V. Fedorov³, V. N. Fedosseev¹¹, D. A. Fink,^{11,10} L. P. Gaffney^{4,11,§} L. Ghys,^{4,||} R. D. Harding,^{1,11} M. Huyse,⁴ N. Imai,¹² D. T. Joss,¹³ S. Kreim,^{11,10} D. Lunney^{14,¶}, K. M. Lynch,^{7,11} V. Manea^{10,¶}, B. A. Marsh¹¹, Y. Martinez Palenzuela,^{4,11} P. L. Molkanov,³ D. Neidherr,¹⁵ G. G. O'Neill,¹³ R. D. Page,¹³ S. D. Prosyak³, M. Rosenbusch,^{16,**} R. E. Rossel,^{11,17} S. Rothe,^{11,17} L. Schweikhard,¹⁶ M. D. Seliverstov,³ S. Sels,⁴ L. V. Skripnikov³, A. Stott,¹ C. Van Beveren,⁴ E. Verstraelen,⁴ A. Welker,^{11,18} F. Wienholtz,^{11,16,††} R. N. Wolf^{10,16,‡‡} and K. Zuber¹⁸

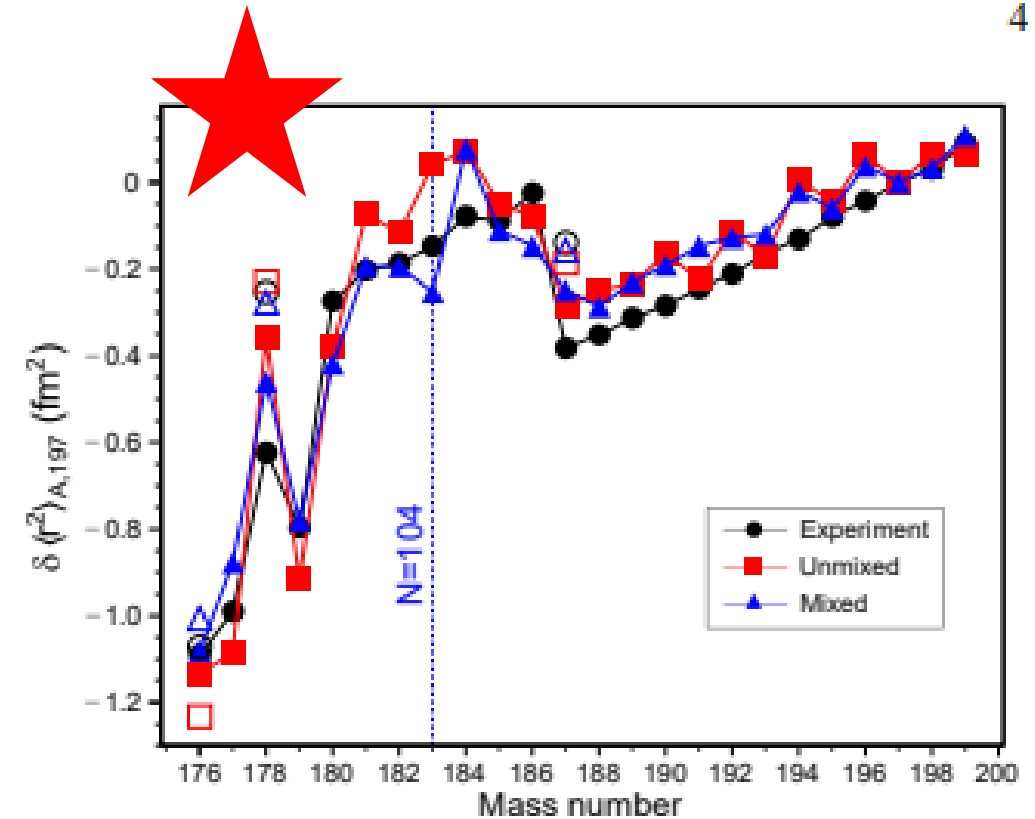


FIG. 2. Comparison between experimental $\delta\langle r^2 \rangle_{A,197}$ values (●) for gold isotopes with HFB calculations without (■) and with (▲) CM included. The filled symbols connected by lines indicate ground states, whilst the hollow symbols represent the isomers in $^{178,187}\text{Au}$ and the high-spin state in ^{176}Au . The $11/2^-$ isomers have been excluded for clarity. The vertical, blue, dashed line represents the $N = 104$ mid-shell.

PHYSICAL REVIEW LETTERS

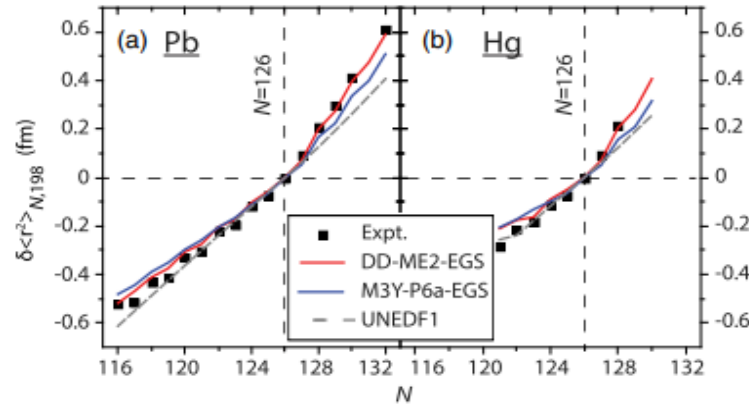


FIG. 3. Panels (a) and (b) show $\delta\langle r^2 \rangle_{N,198}^{A,A'}$ of lead and mercury isotopes relative to ^{208}Pb and ^{206}Hg ($N = 126$), respectively. Experimental mercury data: this Letter and Ref. [16]. Experimental lead data: Ref. [18]. The statistical uncertainties are smaller than the data points. RHB(DD-ME2) results: this Letter. NR-HFB(M3Y-P6a) results: this Letter (mercury) and Ref. [14] (lead). NR-HFB(UNEDF1) results: Ref. [35].

energies of experimental states in model calculations [47,48]. However, it is neglected in the present study since its impact on charge radii is still an open theoretical question.

The results of the RHB and NR-HFB calculations are presented in Fig. 3, together with the experimental results for the lead and mercury chains. In both cases, the kink at $N = 126$ is visibly better reproduced in the RHB (DD-ME2) calculations. To facilitate a quantitative comparison of the experimental and theoretical results, two indicators are employed. OES is quantified considering the isotope's nearest neighbors via the commonly used three-point indicator

ANPH

PHYSICAL REVIEW LETTERS

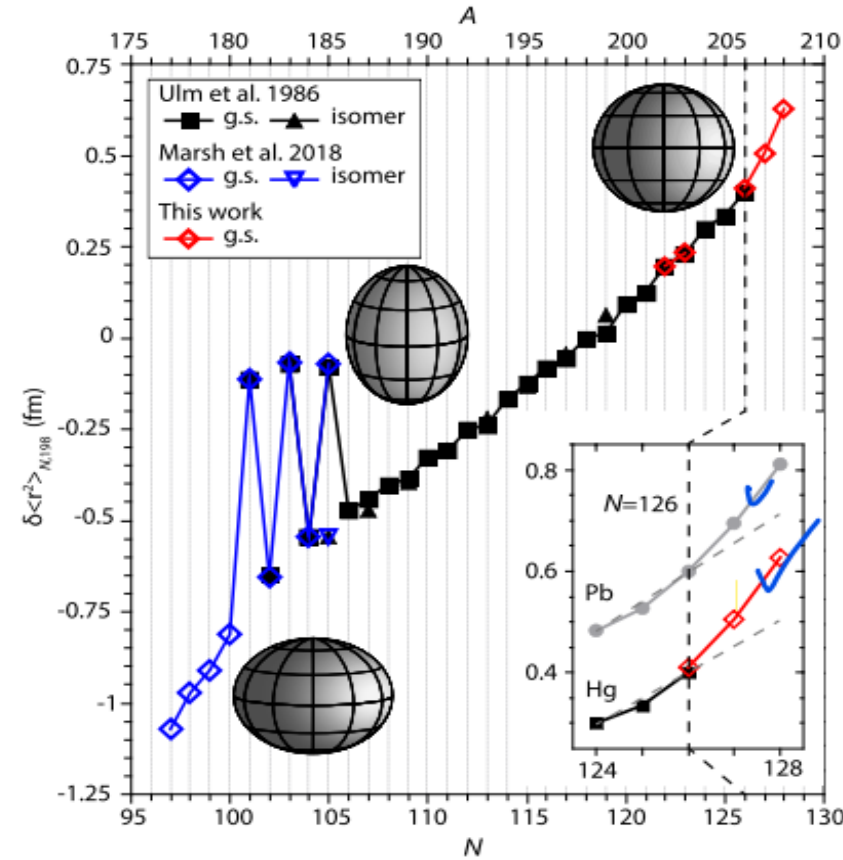


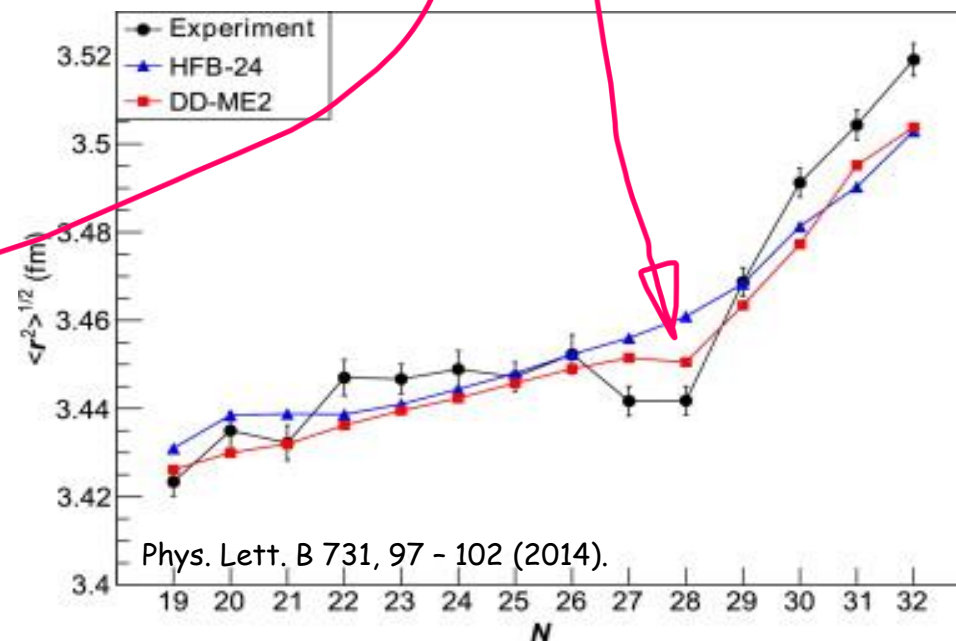
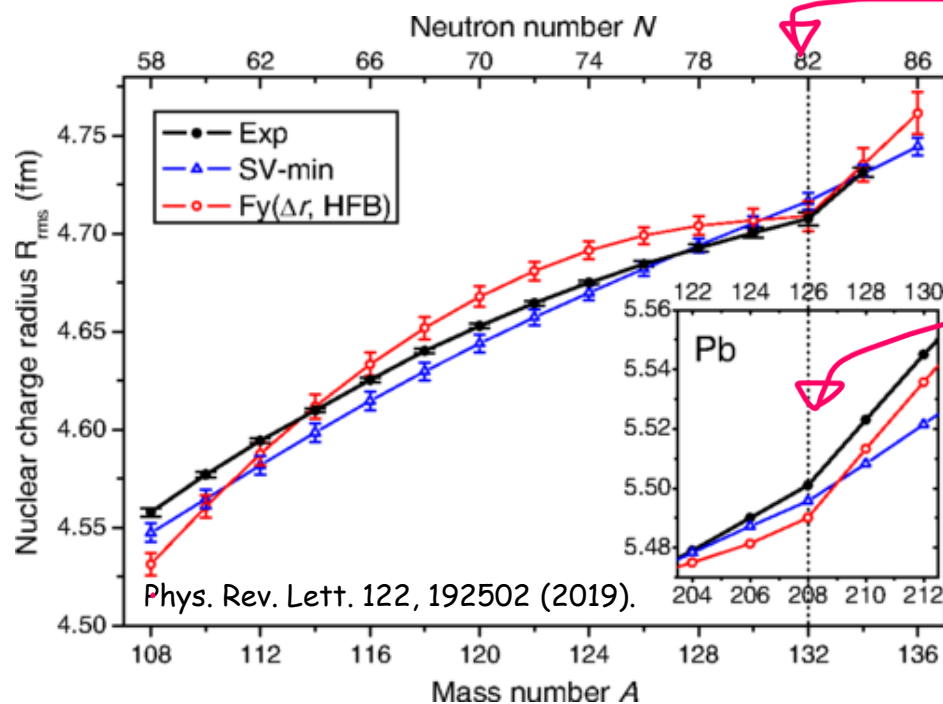
FIG. 1. Systematics of the difference in mercury ground state (g.s.) and isomer mean-square charge radii. Data from the present Letter are shown by red symbols; earlier data are taken from Refs. [16] (black) and [17] (blue). The inset highlights the kink at $N = 126$ and the neighboring OES in both the mercury and lead [18] isotopic chains. The lead isotopes are arbitrarily displaced from those of mercury for clarity. The dashed lines through $N = 124$ and 126 in the inset are added to highlight the kinks. Statistical uncertainties are smaller than the data points.



1. Kink Structure

Kink structures in Sn and K isotopes

- Indeed, charge radii reflect various nuclear structure phenomena such as halo structures, shape staggering and shape coexistence, pairing correlations, neutron skins and the occurrence of nuclear magic numbers.
- The remarkably abrupt changes in charge radii are observed naturally across the neutron-closure shells, namely the kinks at $N = 20, 28, 50, 82, 126$ [1-4].



[1] Gorges, C. et al. Phys. Rev. Lett. 122, 192502 (2019).

[2] Anselment, M. et al. Nucl. Phys. A 451, 471 - 480 (1986).

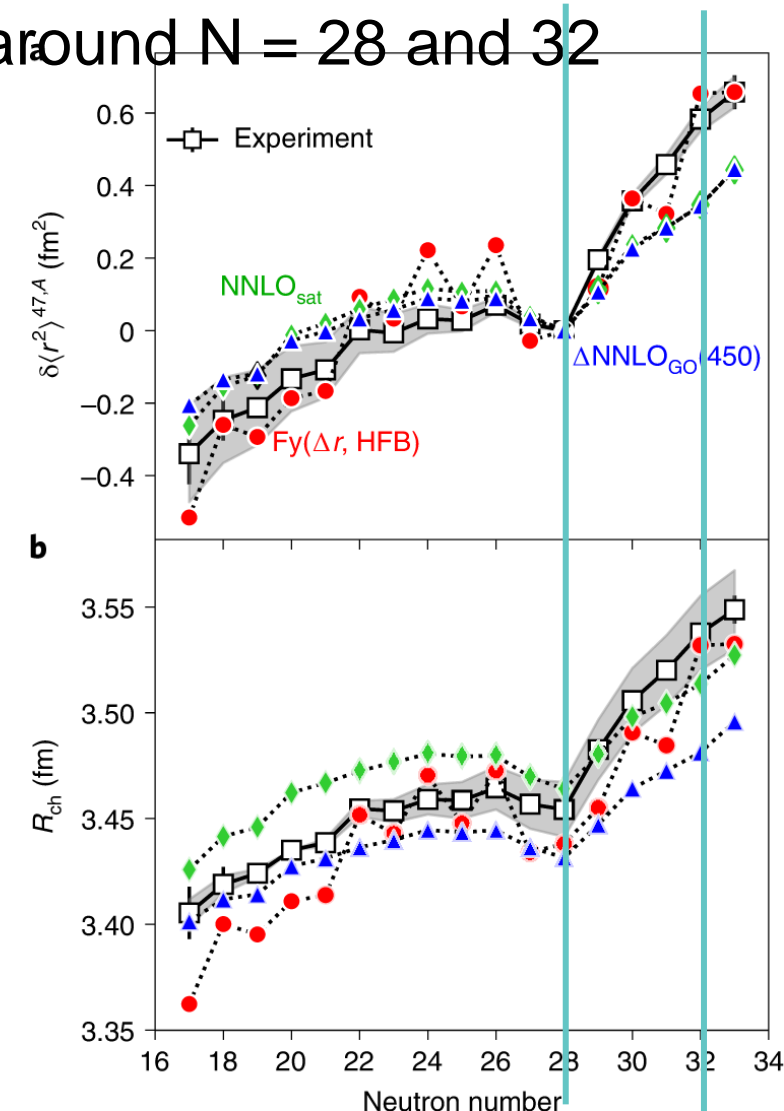
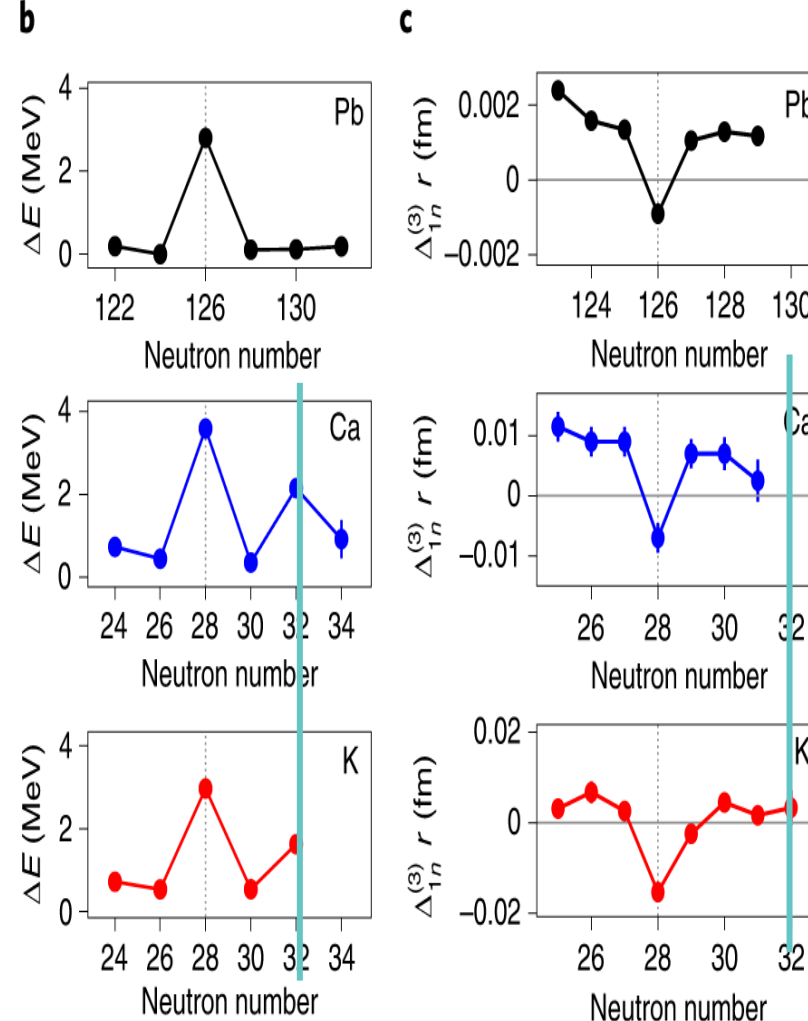
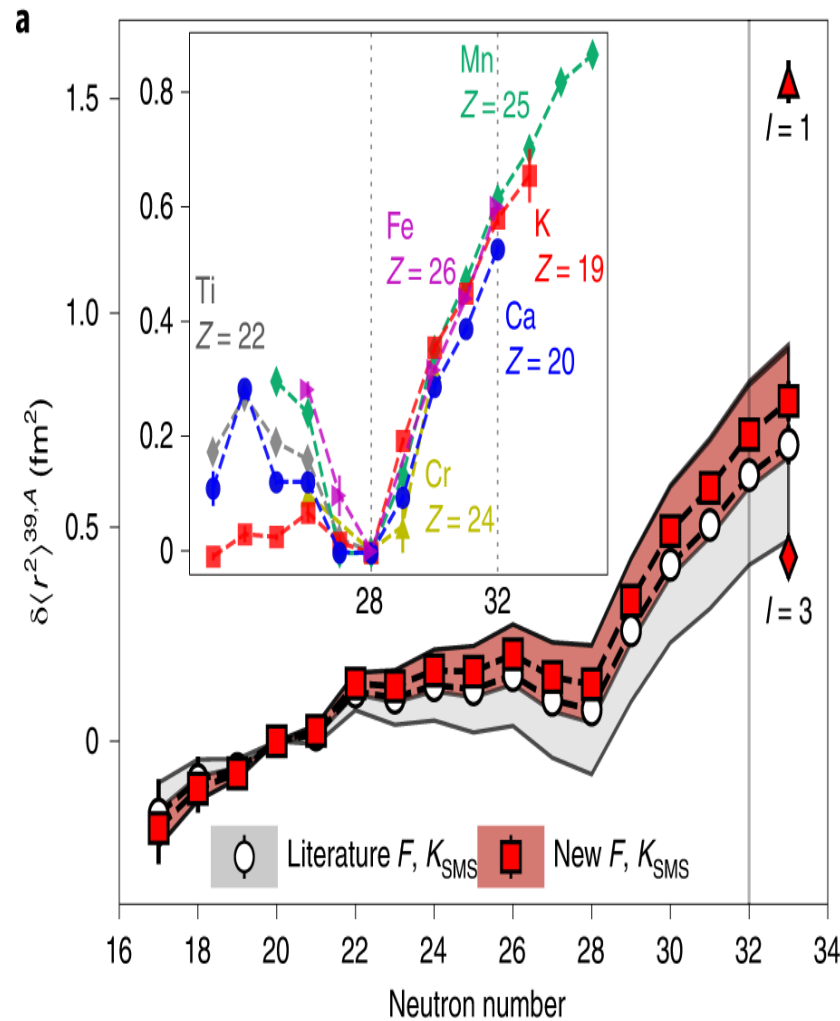
[3] Farooq-Smith, G. J. et al. Phys. Rev. C 96, 044324 (2017).

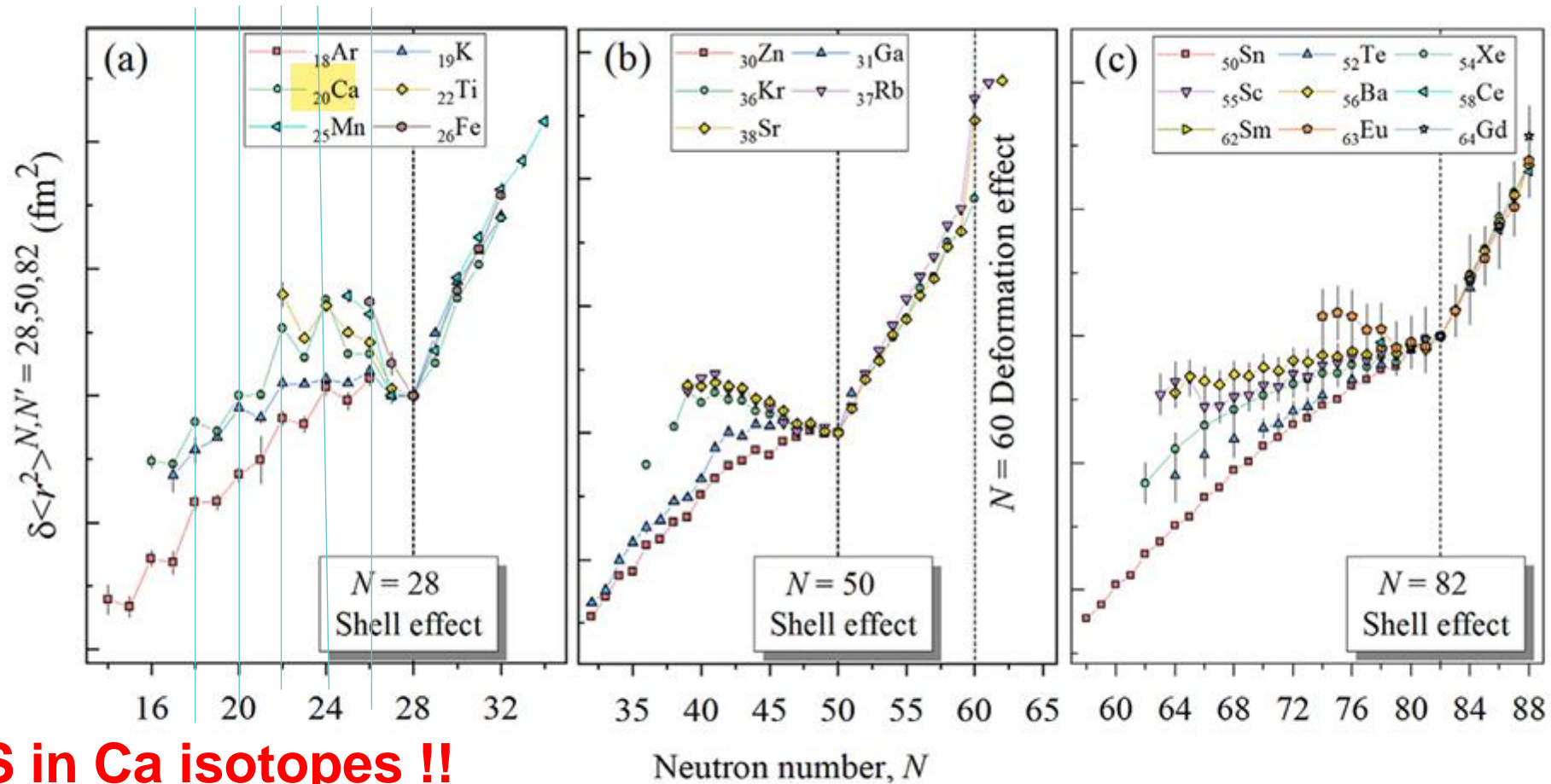
[4] Kreim, K. et al. Phys. Lett. B 731, 97 - 102 (2014).

1. Kink Structure

Kink structures of other nuclei

Relative differences by two-point and three-point of mean square radii and binding energies of light nuclei around $N = 28$ and 32





(Anti-) OES in Ca isotopes !!

Fig. 3.4. Changes in mean-square charge radii in the calcium ($Z = 20$), nickel ($Z = 28$), tin ($Z = 50$) regions, as a function of the neutron number N , with respect to the reference isotope with a magic neutron number. A clear “kink” is commonly observed at neutron magic numbers. Interestingly, the charge radii of neutron-rich nuclei after these neutron magic numbers increase with a similar slope gradient for all proton numbers. This is in contrast to neutron-deficient isotopes, for which the charge radii exhibit a strong dependence upon the proton number.

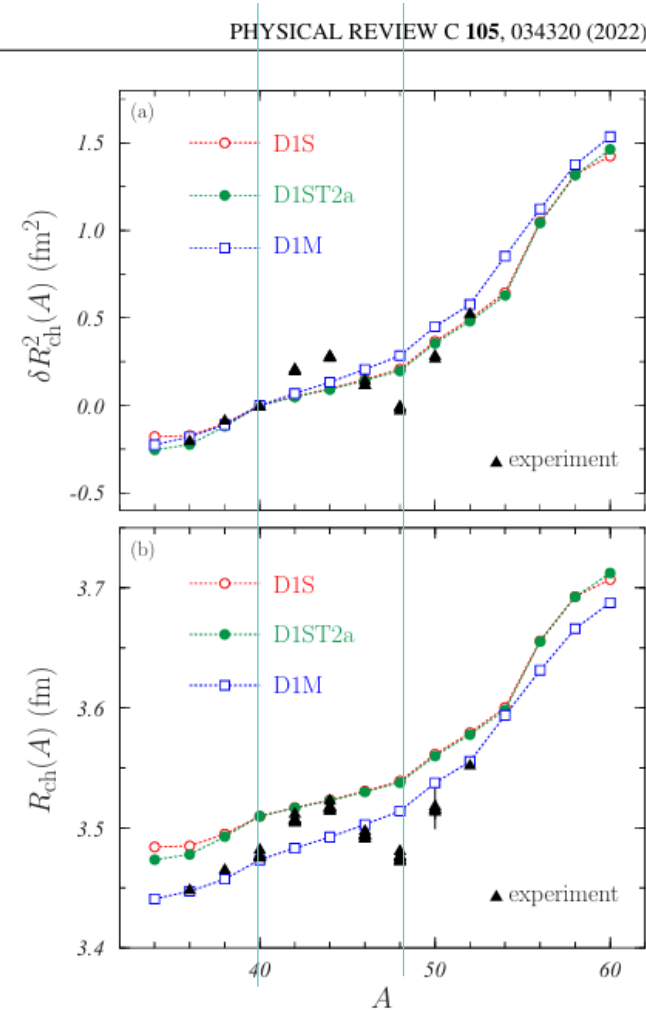


FIG. 3. IPM results obtained with the D1S (open red dots), D1ST2a (solid green dots), and D1M (open blue squares) Gogny interactions for the Ca isotopes considered in our work, with the experimental data (black triangles). (a) Isotope shifts of the squared r.m.s. charge radii evaluated with respect to the ^{40}Ca r.m.s. radius, Eq. (15); the experimental data were obtained from Refs. [1,2,24–26]. (b) r.m.s. charge radii of the Ca isotopes; the experimental values were calculated by considering the experimental isotope shifts shown in panel (a) and the reference r.m.s. charge radius $R_{\text{ch}}(A = 40) = 3.4776(19)$ fm [27].

A Brief summary

Thanks to the recent development of the laser spectroscopy, MR ToP and RI accelerator facilities (and electron scattering) in the world

1. OES in Hg and Au isotopes turns out to be significant compared to any other nuclei, for example, Pb isotopes. **How to understand it ?** and **Anti-OES in Ca isotopes ?**
2. Kink structures appear above any magic shell in light and heavy nuclear isotopes. **How to interpret this behavior ?**
3. We need **a more refined nuclear model**, which needs to explain main properties of the whole nuclei in the nuclear chart by including the relativistic description, deformation, continuum, driplines etc. and also **proper description of odd nuclei**.

Contents

1. Experimental evidences of OES and Kink structures

1-1. Odd-Even (**Shape**) Staggering (OES)

1-2. Kink

2. Deformed Relativistic Hartree Bogoliubov in Continuum (DRHBc) theory and **other DFTs**

Myeong-Hwan Mun, Seonghyun Kim, Myung-Ki Cheoun, W.Y. So, Soonchul Choi, Phys. Lett.B 847, 138298 (2023)

3. OES and Kink of Hg and **Au** by DRHBc and other Skyrme DFTs

3-1. OES of Hg and **Au**

Myeong-Hwan Mun, E. Ha, Y. B. Choi, Myung-Ki Cheoun, PRC 110, 024310 (2024)

3-2. Kink of Hg and Pb

Seonghyun Kim, Myeong-Hwan Mun, Myung-Ki Cheoun and Eunja Ha, PRC 105, 034340 (2022)

4. CM corrections and Magnetic Moments **Y. Tanimura and M. K. Cheoun,**

PRC 109, 054323 (2024)

5. Summary

Theoretical framework for DRHBc

The 7th workshop on nuclear mass table with DRHBc theory

Date: July 1 to 4, 2024

Place: Gangneung Green City Experience Center, Gangneung, Korea

Scientific Contents

- Overview of the DRHBc calculations for odd-Z nuclei
- DRHBc calculations results for odd-Z nuclei
- Progress Reports from PIs for different regions
- Interesting topics of DRHBc mass table
- Future working plan toward a complete DRHBc mass table

Schedule Overview

- July 1, 2024 (Mon)
 - Arrival & Registration / Domestic meeting
- July 2 (Tue)
 - Morning Session / Afternoon Session / Banquet
- July 3 (Wed)
 - Morning Session / Excursion
- July 4 (Thu)
 - Morning Session / Discussions

➤ We start from the following point-coupling Lagrangian density¹

$$\begin{aligned}
 \mathcal{L} = & \bar{\psi}(i\gamma_{\mu}\partial^{\mu} - M)\psi - \frac{1}{2}\alpha_S(\bar{\psi}\psi)(\bar{\psi}\psi) \\
 & - \frac{1}{2}\alpha_V(\bar{\psi}\gamma_{\mu}\psi)(\bar{\psi}\gamma^{\mu}\psi) - \frac{1}{2}\alpha_{TV}(\bar{\psi}\vec{\tau}\gamma_{\mu}\psi)(\bar{\psi}\vec{\tau}\gamma^{\mu}\psi) \\
 & - \frac{1}{2}\alpha_{TS}(\bar{\psi}\vec{\tau}\psi)(\bar{\psi}\vec{\tau}\psi) - \frac{1}{3}\beta_S(\bar{\psi}\psi)^3 \\
 & - \frac{1}{4}\gamma_S(\bar{\psi}\psi)^4 - \frac{1}{4}\gamma_V[(\bar{\psi}\gamma_{\mu}\psi)(\bar{\psi}\gamma^{\mu}\psi)]^2 \\
 & - \frac{1}{2}\delta_S\partial_{\nu}(\bar{\psi}\psi)\partial^{\nu}(\bar{\psi}\psi) - \frac{1}{2}\delta_V\partial_{\nu}(\bar{\psi}\gamma_{\mu}\psi)\partial^{\nu}(\bar{\psi}\gamma^{\mu}\psi) \\
 & - \frac{1}{2}\delta_{TV}\partial_{\nu}(\bar{\psi}\vec{\tau}\gamma_{\mu}\psi)\partial^{\nu}(\bar{\psi}\vec{\tau}\gamma^{\mu}\psi) \\
 & - \frac{1}{2}\delta_{TS}\partial_{\nu}(\bar{\psi}\vec{\tau}\psi)\partial^{\nu}(\bar{\psi}\vec{\tau}\psi) \\
 & - \frac{1}{4}F^{\mu\nu}F_{\mu\nu} - e\bar{\psi}\gamma^{\mu}\frac{1-\tau_3}{2}A_{\mu}\psi,
 \end{aligned}$$

[1] J. Meng (Editor). Relativistic Density Functional for Nuclear Structure (2016)

2. Theoretical Approaches

DRHBc (Relativistic MF approach with point coupling)

$$\begin{aligned} \mathcal{L} = & \bar{\psi}(i\gamma_\mu\partial_\mu - M)\psi - \frac{1}{2}\alpha_s(\bar{\psi}\psi)(\bar{\psi}\psi) - \frac{1}{2}\alpha_V(\bar{\psi}\gamma_\mu\psi)(\bar{\psi}\gamma^\mu\psi) - \frac{1}{2}\alpha_{TV}(\bar{\psi}\vec{\tau}\gamma_\mu\psi)(\bar{\psi}\vec{\tau}\gamma^\mu\psi) \\ & - \frac{1}{2}\alpha_{TS}(\bar{\psi}\vec{\tau}\psi)(\bar{\psi}\vec{\tau}\psi) - \frac{1}{3}\beta_S(\bar{\psi}\psi)^3 - \frac{1}{4}\gamma_S(\bar{\psi}\psi)^4 - \frac{1}{4}\gamma_V[(\bar{\psi}\gamma_\mu\psi)(\bar{\psi}\gamma^\mu\psi)]^2 \\ & - \frac{1}{2}\delta_S\partial_\nu(\bar{\psi}\psi)\partial^\nu(\bar{\psi}\psi) - \frac{1}{2}\delta_V\partial_\nu(\bar{\psi}\gamma_\mu\psi)\partial^\nu(\bar{\psi}\gamma^\mu\psi) - \frac{1}{2}\delta_{TV}\partial_\nu(\bar{\psi}\vec{\tau}\gamma_\mu\psi)\partial^\nu(\bar{\psi}\vec{\tau}\gamma^\mu\psi) \\ & - \frac{1}{2}\delta_{TS}\partial_\nu(\bar{\psi}\vec{\tau}\psi)\partial^\nu(\bar{\psi}\vec{\tau}\psi) - \frac{1}{4}F^{\mu\nu}F_{\mu\nu} - e\bar{\psi}\gamma^\mu\frac{1-\tau_3}{2}A_\mu\psi, \end{aligned} \quad (1)$$

where M is the nucleon mass, e is the **proton charge**, and A_μ and $F_{\mu\nu}$ are the **four-vector potential** and **field tensor of the electromagnetic field**, respectively. The coupling constant α_i for four-fermion terms is specified by superscripts ($i = S, V$ and T) which stand for the scalar, vector, and isovector channels, respectively. The higher-order terms are specified by β_i and γ_i , while δ_i refers to gradient terms. The isovector-scalar channels, α_{TS} and δ_{TS} , are neglected in the DRHBc approach [22]. The EDF is derived in terms of nucleon scalar density, $\rho_s(\mathbf{r}) = \sum_{i=1}^A \bar{\psi}_i(\mathbf{r})\psi_i(\mathbf{r})$, and **IS and IV** currents $j_\mu(\mathbf{r}) = \sum_{i=1}^A \bar{\psi}_i(\mathbf{r})\gamma_\mu\psi_i(\mathbf{r})$, and $\vec{j}_\mu(\mathbf{r}) = \sum_{i=1}^A \bar{\psi}_i(\mathbf{r})\vec{\tau}\gamma_\mu\psi_i(\mathbf{r})$ as follows [17, 41]

$$\begin{aligned} E_{RMF}[\psi, \bar{\psi}, A_\mu] = & \sum_{i=1}^A \int d^3\mathbf{r} \psi_i^\dagger(\boldsymbol{\alpha} \cdot \mathbf{p} + \beta M)\psi_i - \frac{1}{2}(\nabla \cdot \mathbf{A})^2 + \frac{1}{2}e \int d^3\mathbf{r} j_p^\mu A_\mu \\ & + \int d^3\mathbf{r} [\frac{1}{2}(\alpha_S\rho_s^2 + \alpha_V j^\mu j_\mu + \alpha_{TV} \vec{j}^\mu \cdot \vec{j}_\mu) + \frac{1}{3}\beta_S\rho_s^3 + \frac{1}{4}\gamma_S\rho_s^4 \\ & + \frac{1}{4}\gamma_V(j^\mu j_\mu)^2 + \frac{1}{2}\delta_S\rho_s\Box\rho_s + \frac{1}{2}\delta_V j^\mu\Box j_\mu + \frac{1}{2}\delta_{TV} \vec{j}^\mu \cdot \Box \vec{j}_\mu]. \end{aligned} \quad (2)$$

The present calculations are carried out by **solving** the HB equation with the density functional PC-PK1 [47], which reads [41]

$$\int d^3\mathbf{r}' \begin{pmatrix} h_D(\mathbf{r}, \mathbf{r}') - \lambda_\tau & \Delta(\mathbf{r}, \mathbf{r}') \\ -\Delta^*(\mathbf{r}, \mathbf{r}') & -h_D^*(\mathbf{r}, \mathbf{r}') + \lambda_\tau \vec{j}^\mu \cdot \vec{j}_\mu \end{pmatrix} \begin{pmatrix} U_k(\mathbf{r}) \\ V_k(\mathbf{r}) \end{pmatrix} = E_k \begin{pmatrix} U_k(\mathbf{r}) \\ V_k(\mathbf{r}) \end{pmatrix}, \quad (3)$$

where λ_τ is the Fermi energy ($\tau = n/p$) for neutrons or protons. E_k and $(U_k, V_k)^T$ are the quasiparticle energy and quasiparticle wave function. In coordinate space, the Dirac Hamiltonian h_D is given by

$$h_D(\mathbf{r}, \mathbf{r}') = [\boldsymbol{\alpha} \cdot \mathbf{p} + V(\mathbf{r}) + \beta(M + S(\mathbf{r}))]\delta(\mathbf{r}, \mathbf{r}'), \quad (4)$$

where M is the nucleon mass, and $V(\mathbf{r})$ and $S(\mathbf{r})$ are the vector and scalar potentials, respectively, given by

$$S(\mathbf{r}) = \alpha_S\rho_S + \beta_S\rho_S^2 + \gamma_S\rho_S^3 + \delta_S\Delta\rho_S, \quad (5)$$

$$V(\mathbf{r}) = \alpha_V\rho_V + \gamma_V\rho_V^3 + \delta_V\Delta\rho_V + eA^0 + \alpha_{TV}\tau_3\rho_3 + \delta_{TV}\tau_3\Delta\rho_3,$$

with the following densities represented **in terms of the quasiparticle wave functions as follows**

$$\rho_S(\mathbf{r}) = \sum_{k>0} \bar{V}_k(\mathbf{r})V_k(\mathbf{r}), \quad \rho_V(\mathbf{r}) = \sum_{k>0} \bar{V}_k(\mathbf{r})\gamma_0 V_k(\mathbf{r}), \quad \rho_3(\mathbf{r}) = \sum_{k>0} \bar{V}_k(\mathbf{r})\gamma_0\tau_3 V_k(\mathbf{r}). \quad (6)$$

The pairing potential $\Delta(\mathbf{r}, \mathbf{r}')$ is given by the following gap equation in terms of the pairing tensor $\kappa(\mathbf{r}, \mathbf{r}')$ [30]

$$\Delta(\mathbf{r}, \mathbf{r}') = V^{pp}(\mathbf{r}, \mathbf{r}')\kappa(\mathbf{r}, \mathbf{r}'), \quad \kappa(\mathbf{r}, \mathbf{r}') (= \langle |a_k a_{k'}| \rangle) = \sum_{k>0} V_k^*(\mathbf{r})U_k^T(\mathbf{r}'), \quad (7)$$

where we **did not write explicitly** the sum on the spin degree of freedom and the upper and lower components of Dirac spinors. The DRHBc approach uses a density-dependent zero-range force

$$V^{pp}(\mathbf{r}, \mathbf{r}') = \frac{V_0}{2}(1 - P_\sigma)\delta(\mathbf{r} - \mathbf{r}')(1 - \frac{\rho(\mathbf{r})}{\rho_{\text{sat}}}), \quad (8)$$

where ρ_{sat} is the nuclear saturation density, V_0 is the pairing strength, and $(1 - P_\sigma)/2$ is the projector for the **spin-singlet**, $S = 0$ component in the pairing channel. Then the pairing potential and pairing tensor of Eq. (7) become **local quantities** [30],

$$\Delta(\mathbf{r}) = V_0(1 - \rho(\mathbf{r})/\rho_{\text{sat}})\kappa(\mathbf{r}), \quad \kappa(\mathbf{r}) = \sum_{k>0} V_k^+(\mathbf{r})U_k(\mathbf{r}) \quad (9)$$

because of the zero-range and spin-singlet properties of the pairing force in Eq. (8). For the non-local and spin-triplet (isoscalar) interactions, one needs a more careful treatment of the pairing potential and pairing tensor [41].

2. Theoretical Approaches

DRHBc (Relativistic MF approach with point coupling)

Finally, the total energy of a nucleus including the pairing energy and the c.o.m. correction is defined by

$$E_{\text{tot+cm}} = E_{\text{EDF}} + E_{\text{pair}} + E_{\text{cm}}, \quad (10)$$

PHYSICAL REVIEW C **102**, 024314 (2020)

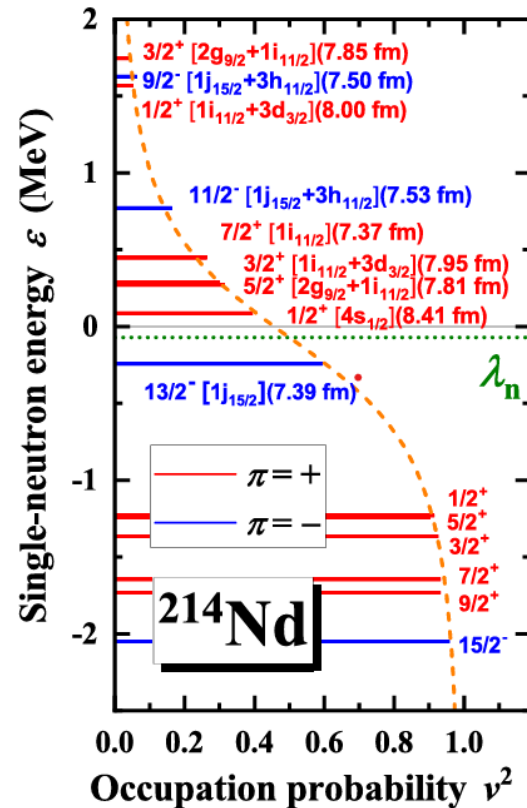


FIG. 14. Single-neutron levels around the Fermi energy in the canonical basis for ^{214}Nd versus the occupation probability v^2 in the DRHBc calculations. Each level is labeled by the quantum numbers m^π . The main components and rms radii for the levels with $\epsilon > -0.3$ MeV are also given. The neutron Fermi energy λ_n is shown with the dotted line. The occupation probability from the BCS formula with the average pairing gap is given by the dashed line. The thin solid line represents the **continuum** threshold.

where E_{EDF} can be expressed with the quasiparticle energies E_k and wave functions of Eq. (3) as

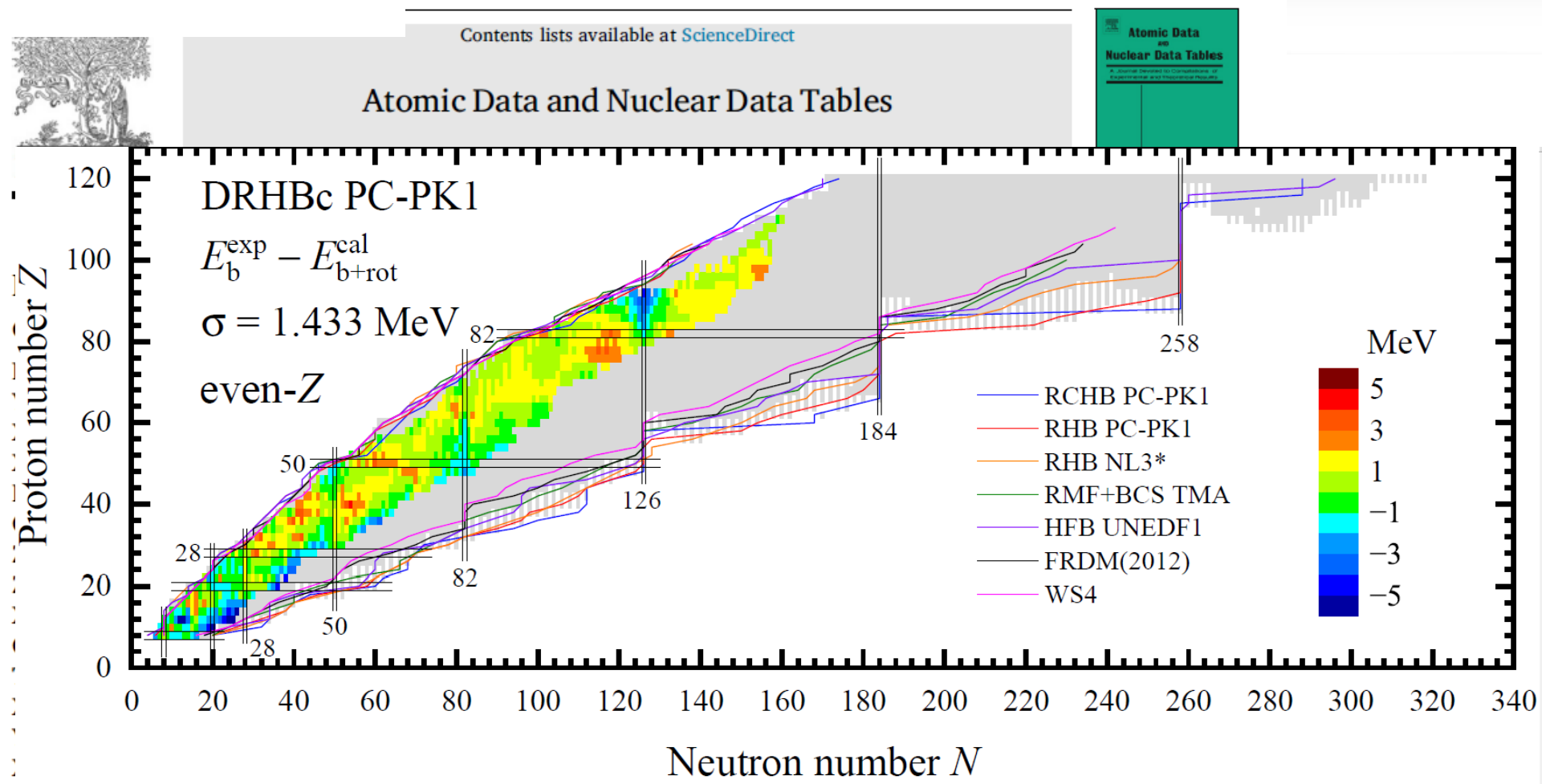
$$E_{\text{EDF}} = \sum_{k>0} \int d^3\mathbf{r} (\lambda_\tau - E_k) V_k^+(\mathbf{r}) V_k(\mathbf{r}) - \int d^3\mathbf{r} \left(\frac{1}{2} \alpha_S \rho_S^2 + \frac{1}{2} \alpha_V \rho_V^2 + \frac{1}{2} \alpha_{TV} \rho_{TV}^2 + \frac{2}{3} \beta_S \rho_S^3 + \frac{3}{4} \gamma_S \rho_S^4 + \frac{3}{4} \gamma_V \rho_V^4 + \frac{1}{2} \delta_S \rho_S \Delta \rho_S + \frac{1}{2} \delta_V \rho_V \Delta \rho_V + \frac{1}{2} \delta_{TV} \rho_{TV} \Delta \rho_{TV} + \frac{1}{2} \rho_p e A^0 \right) - 2E_{\text{pair}}. \quad (11)$$

We note that this EDF can be derived for general HFB energy, as derived in Appendix A.

In the DRHBc approach [48], the pairing energy E_{pair} , with the zero-range pairing force, is given by the pairing potential and pairing tensor as follows [48]

$$E_{\text{pair}} = -\frac{1}{2} \int d^3\mathbf{r} \kappa(\mathbf{r}) \Delta(\mathbf{r}). \quad (12)$$

For the pairing strength, we use $V_0 = -325.0$ MeV fm³. The saturation density is adopted as $\rho_{\text{sat}} = 0.152$ fm⁻³ together with a pairing window of 100 MeV. The energy cutoff $E_{\text{cut}}^+ = 300$ MeV, and the angular momentum cutoff $J_{\text{max}} = (23/2)\hbar$, are taken for the Dirac Woods-Saxon basis. The above numerical details are the same as those suggested in Refs. [22, 23] for the DRHBc mass table calculation. For the present calculation, the Legendre expansion truncation is chosen as $\lambda_{\text{max}} = 8$ [22, 23].



Qiang Zhao²¹, Yingchun Zhao¹, Ruyou Zheng¹³, Chang Zhou¹, Shan-Gui Zhou^{26,41,31,14},
Lianjian Zou¹⁹, DRHBc Mass Table Collaboration

PC-PK1 + DRHBc : 4829 bound even-Z nuclei with $8 \leq Z \leq 120$ DRHBc Collaboration,

At. Data Nucl. Data Tables 144, 101488 (2022);158, 101661 (2024)

ANPHA Symposium, Huizhou, Guangdong, China, Nov. 15

Contents

1. Experimental evidences of OES and Kink structures

1-1. Odd-Even (**Shape**) Staggering (OES)

1-2. Kink

2. Deformed Relativistic Hartree Bogoliubov in Continuum (DRHBc) theory and other DFTs

Myeong-Hwan Mun, Seonghyun Kim, Myung-Ki Cheoun, W.Y. So, Soonchul Choi, Phys. Lett.B 847, 138298 (2023)

3. OES and Kink of Hg and Au by DRHBc and other Skyrme DFTs

3-1. OES of Hg and Au

Myeong-Hwan Mun, E. Ha, Y. B. Choi, Myung-Ki Cheoun, PRC 110, 024310 (2024)

3-2. Kink of Hg and Pb

Seonghyun Kim, Myeong-Hwan Mun, Myung-Ki Cheoun and Eunja Ha, PRC 105, 034340 (2022)

4. CM corrections and Magnetic Moments

Y. Tanimura and M. K. Cheoun, PRC 109, 054323 (2024)

5. Summary

3. OE Shape Staggering Results

Total Binding Energy in **Hg, Au and Pb** isotopes

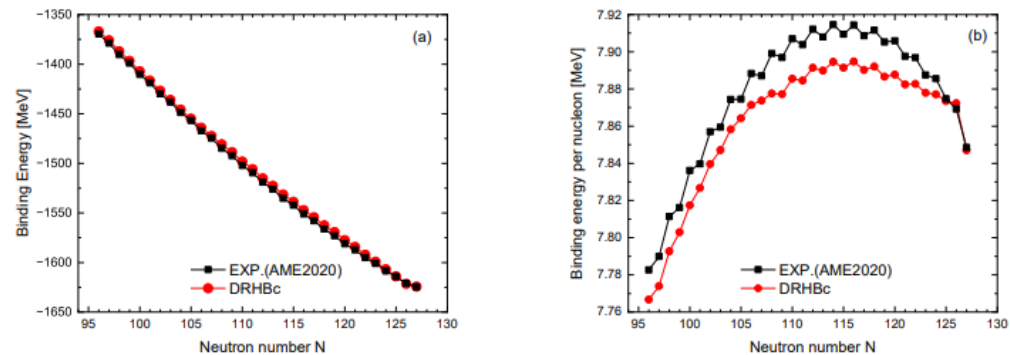
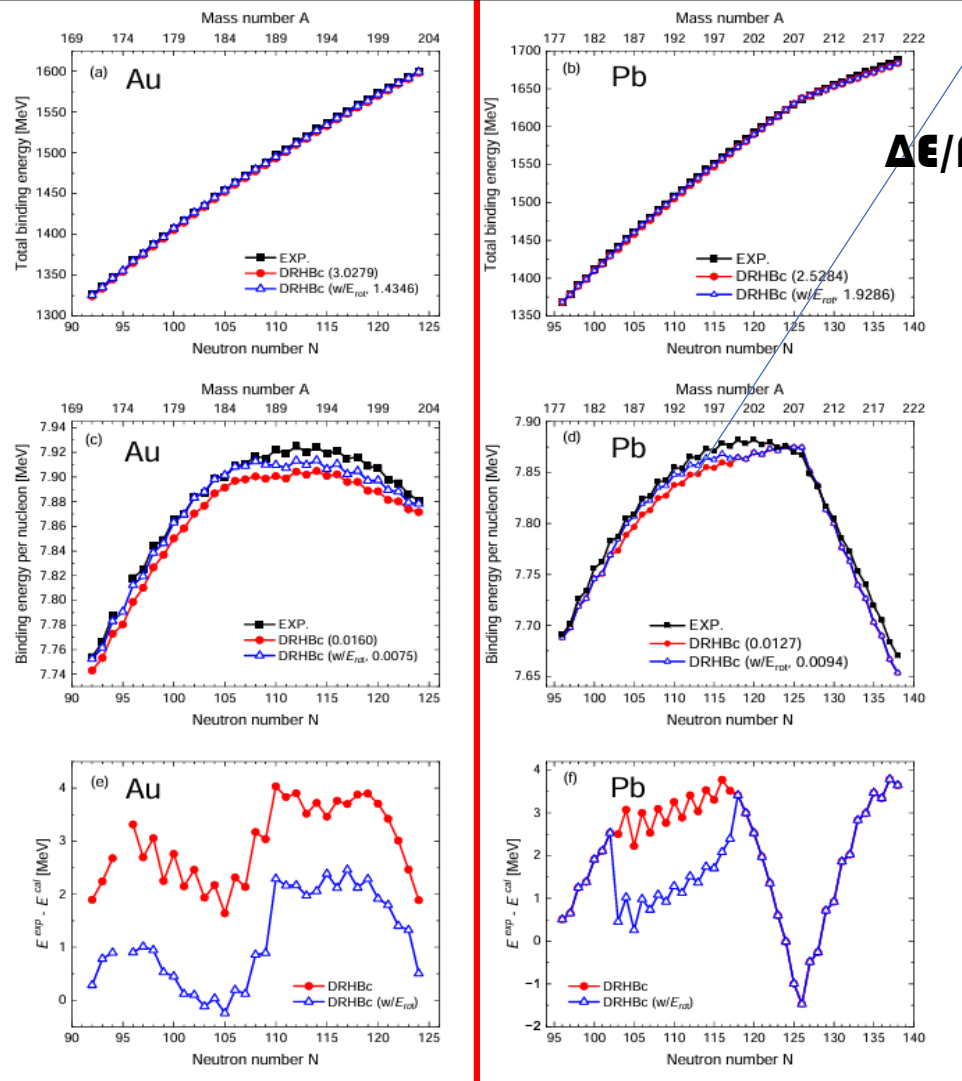


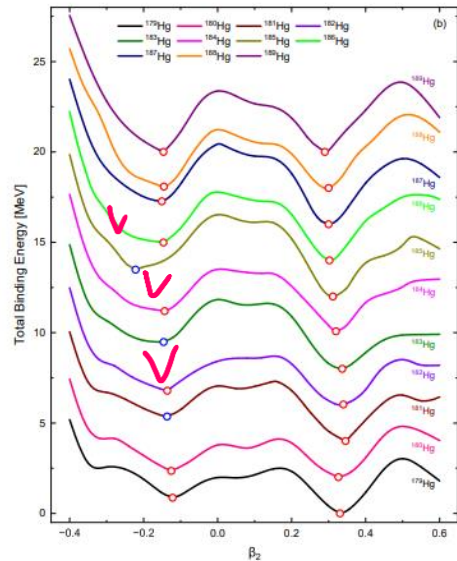
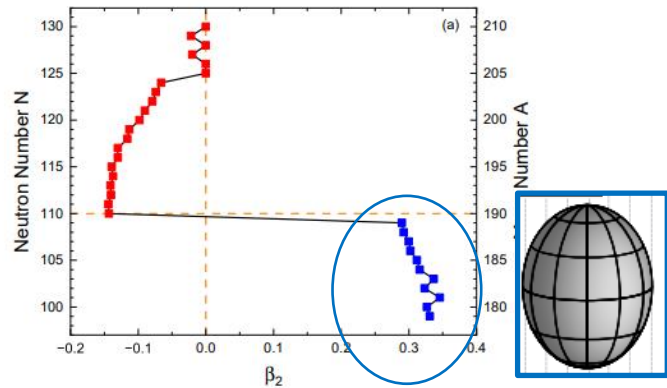
FIG. 3: (Color online) TBEs (a) and BE per nucleon (b) of Hg isotopes ($N = 96 - 127$) determined from DRHBc mass model. They are compared with the available experimental data taken from [55].



$\Delta E/A < 0.02 \text{ MeV} !!!$

FIG. 1: (Color online) PECs (a)((b)), BE/A (c)((d)) Au (Pb) isotopes determined by DRHBc calculations without (red circles) and with (blue triangles) rotational correction E_{rot} . They are compared with available experimental data taken from Ref. [101]. The numbers in parentheses stand for average rms deviation in MeV to the data [101]. **The relative difference between the experimental TBE data and the DRHBc calculations are enlarged in the panel (e) and (f), respectively, for Au and Pb isotopes.**

3. OE Shape Staggering Results Potential Energy Curve Evolution with Deform. for **Hg**



Shape Coexistence
around $N = 100$

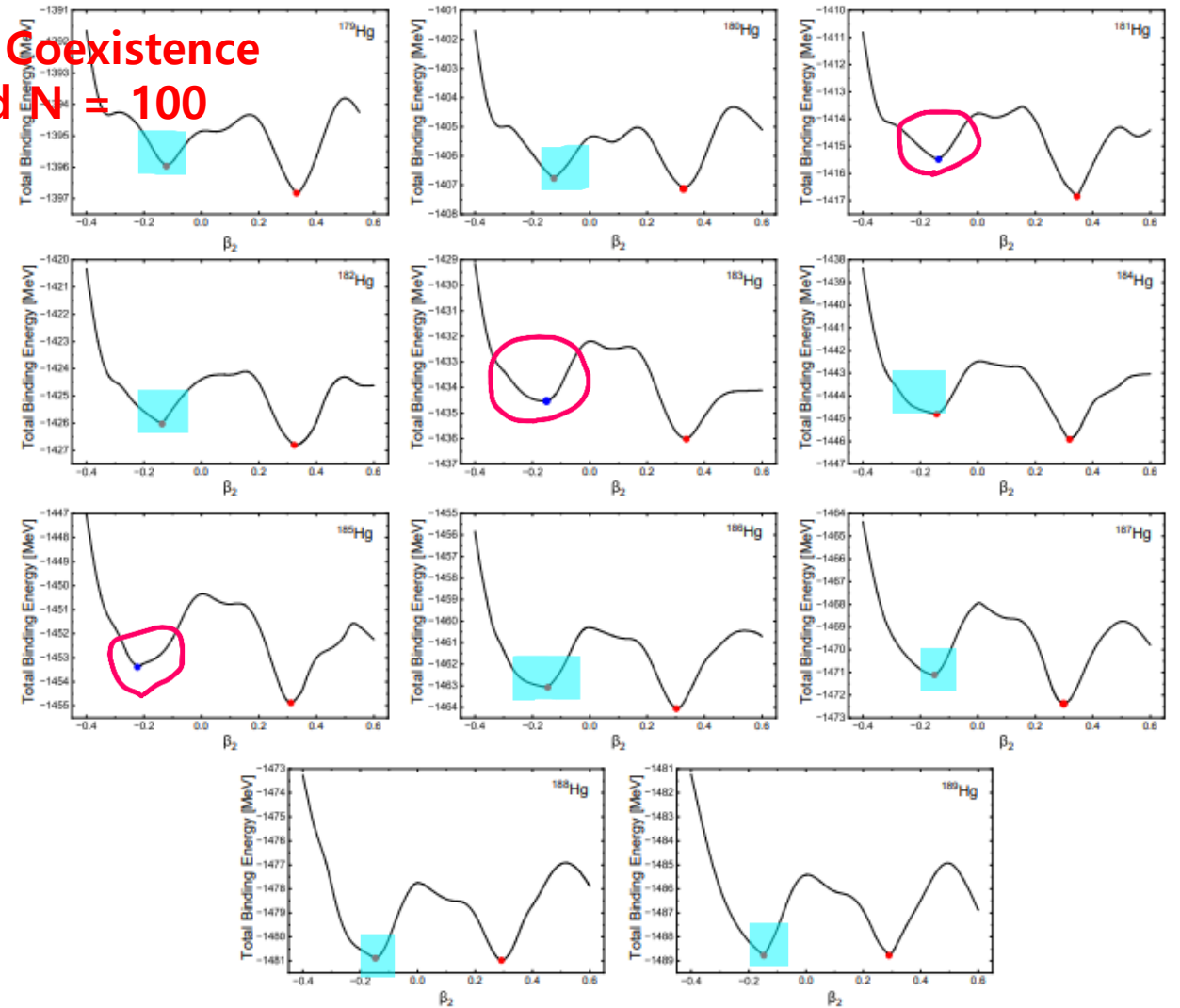


FIG. 1: (Color online) Deformation parameters β_2 of Hg isotopes ($A = 179 - 210$) by DRHBc mass model (a). Total binding energies (TBEs) of some Hg isotopes ($A = 179 - 189$) in the prolate region (b). All of the Hg isotopes in this mass region show a possibility of the shape coexistence whose energy differences are within 1 MeV maximally although exact calculations provide a prolate deformation. Blue points of $^{181,183,185}\text{Hg}$ indicate oblate deformations in a local minimum. Detailed TBEs are shown in Fig. 2.

FIG. 2: (Color online) Detailed TBE curves in terms of the deformation parameter β_2 for $^{179-189}\text{Hg}$ isotopes. The blue points in oblate region for $^{181,183,185}\text{Hg}$ disclose local minima of the TBEs, that is, they are located a bit higher than 1 MeV compared to those in prolate deformation.

3. OE Shape Staggering Results

Potential Energy Curve Evolution with Deform. for Au

Evolution of TBEs with deformation by DRHBC for ^{79}Au

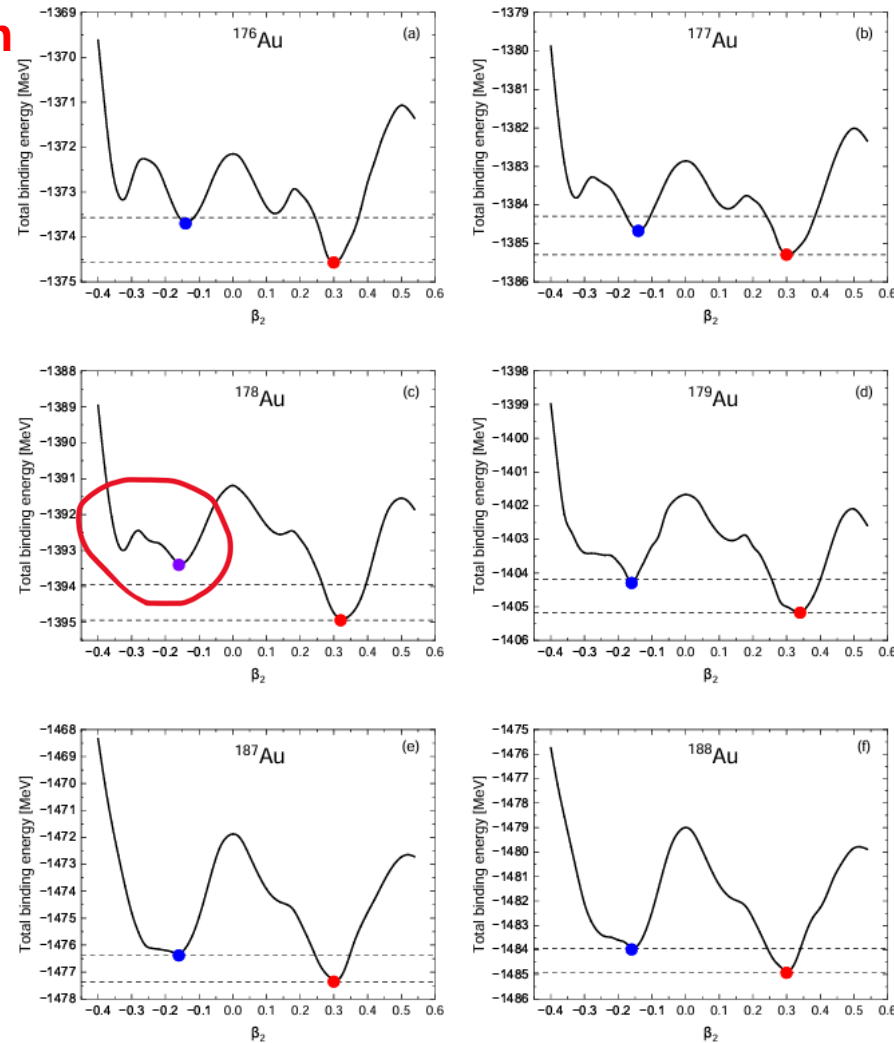
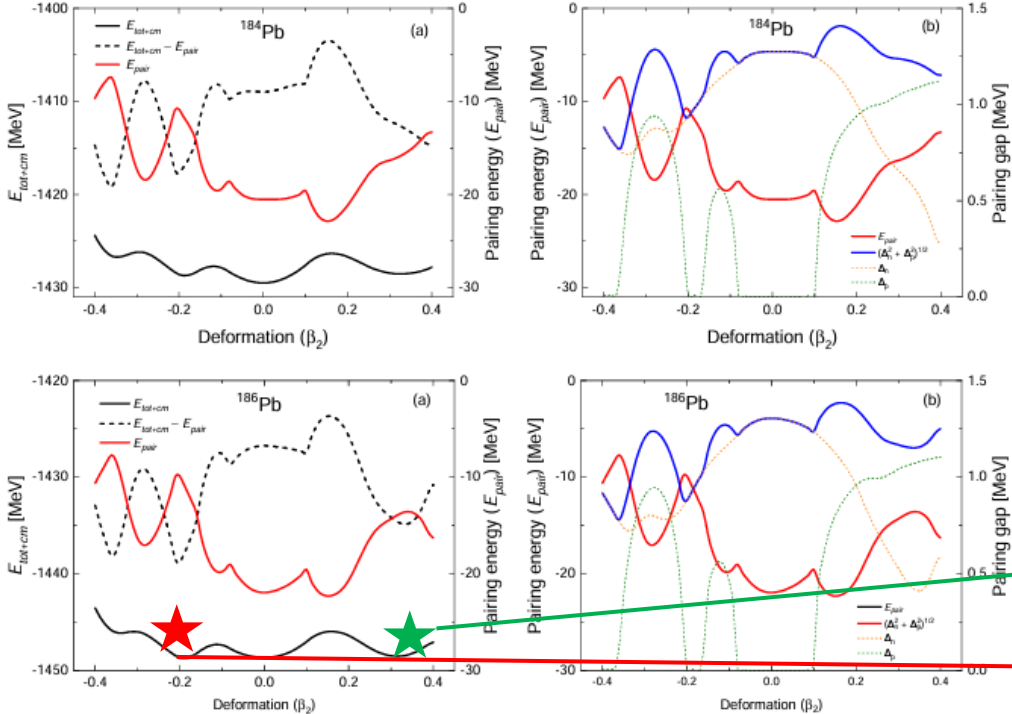


FIG. 4: (Color online) Detailed **PECs** in terms of the deformation parameter β_2 for $^{176-179}\text{Au}$ and $^{187,188}\text{Au}$ isotopes. All of the isotopes demonstrate a possibility of the shape coexistence coming from about 1 MeV energy difference between prolate and oblate minima. **But, the violet point** in oblate region in the panel (c) for ^{178}Au is located a bit higher than 1 MeV compared to **the** prolate deformation.

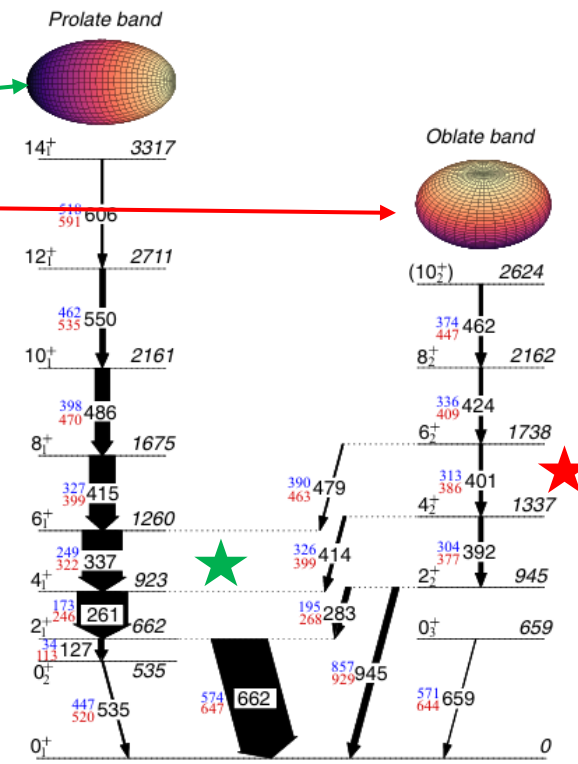
Shape Coexistence of Pb isotopes

186Pb and Rotational Band and Pairing



In Fig. 3, we provide the results for some specific nuclei, $^{184,186}\text{Pb}$, which discloses the possibility of the shape coexistence [52]. Similar evolution pattern to the results in the spherical and oblate cases in Fig. 1 and 2 are also found for the mean field energy, pairing

(b) in Fig. 3 shows the larger pairing energy in the prolate region (see their absolute value of the red solid curves) than that in the oblate region, which means the lower moment of inertia by the pairing energy, and consequently the larger energy gap in the rotational banding structures is expected. This is quite consistent with the experimental data [6].



Prolate
=> Larger Pairing
=> Smaller MOI
=> Larger Energy width

FIG. 3: (Color online) Same as Fig. 1, but for possible candidates of shape coexistence nuclei, $^{184,186}\text{Pb}$ isotopes

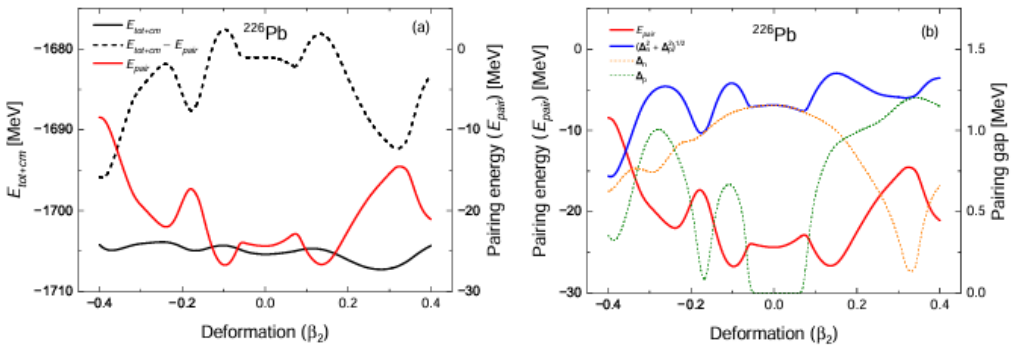


Fig. 3 Partial level scheme of ^{186}Pb presenting transitions relevant to the present work. The widths of the arrows are proportional to the total transition intensities. The K- and L-conversion electron energies have been

3. OE Shape Staggering Results Nuclear Shape Transition of Hg isotopes

Blue points are obtained by DRHBc w/o considering shape coexistence !

=> We could not explain the OES data as well as small charge radii !!

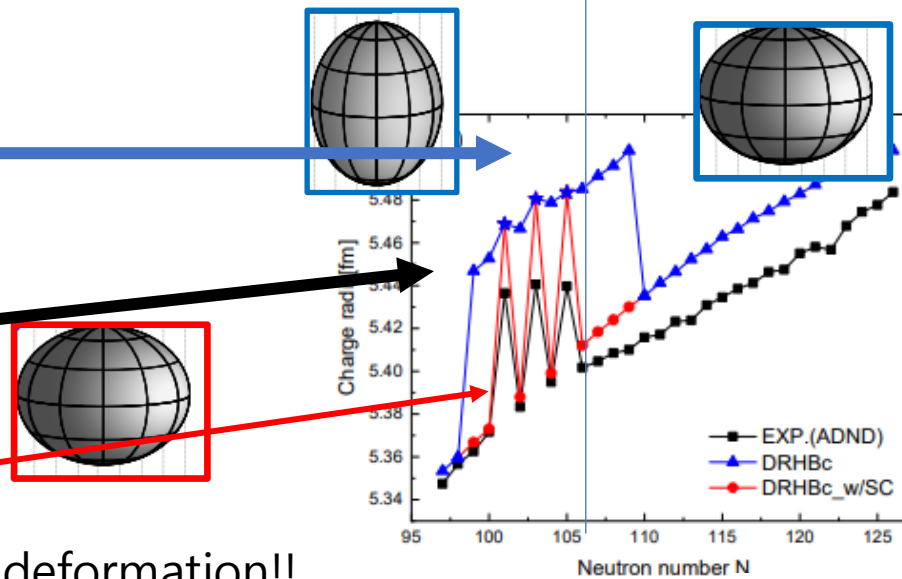
If we take into account the shape coexistence, we obtained the red points by oblate deformation!!

=> Can explain small charge radii !!

But still, we cannot explain the OES data of 181,183 and 185 of Hg.

However, remember the oblate minima of 181,183,185 of Hg are 2nd local minima. We have to take prolate deformation.

Then the OES (blue stars) can be explained clearly by red lines.



$$\delta \langle r^2 \rangle^{A,A'} = \langle r^2(A) \rangle - \langle r^2(A') \rangle = r_{ch}^2(A) - r_{ch}^2(A')$$

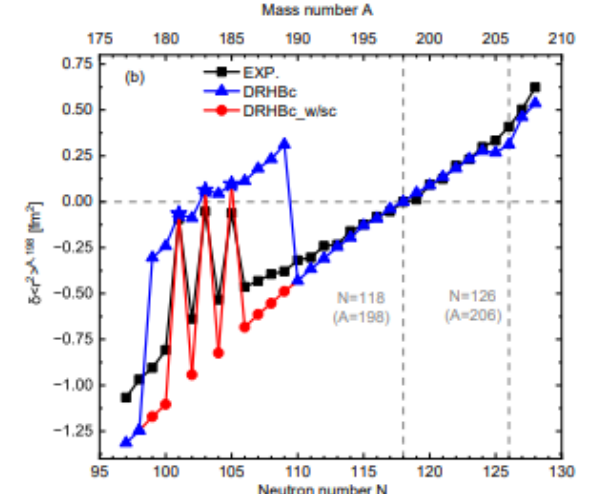


FIG. 4: Shape Coexistence

$$\delta \langle r^2 \rangle^{A,A'}$$

by prolat

by oblate

181,183,185

that we d

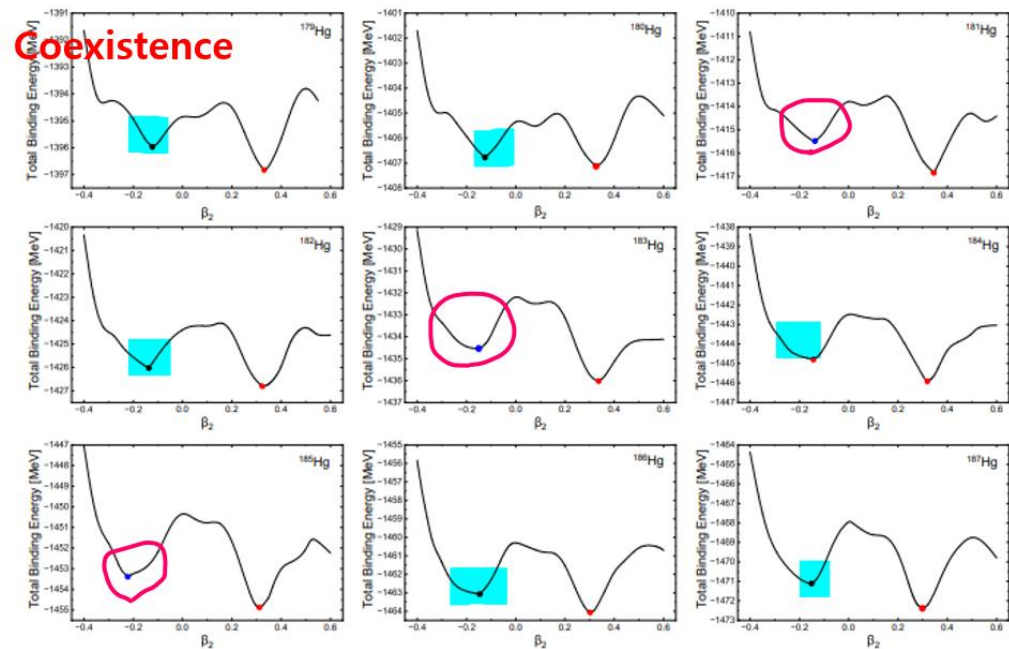
the defor

boxes (le

(right) fo

ANPHA Symposium, H

15-16, 2024



large radii

are obtained

calculated

ie stars for

high means

along with

108. Black

black stars

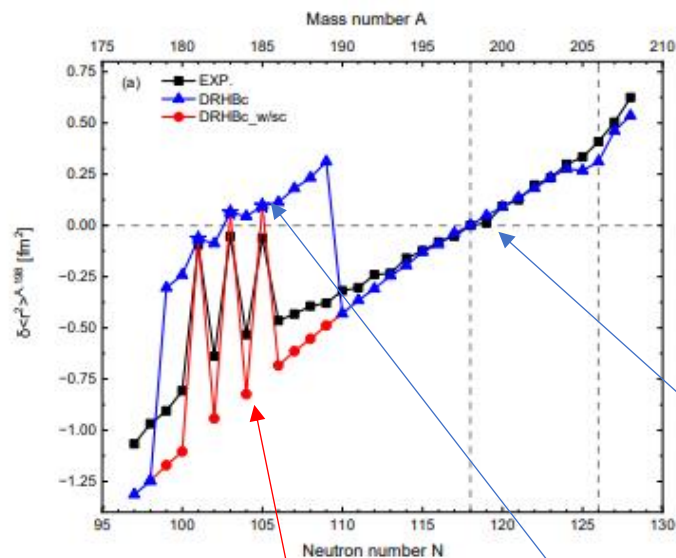


FIG. 3. (Color online) Relative changes of mean square charge radii $\delta \langle r^2 \rangle^{A,198}$ of Hg isotopes. Black boxes stand for the data [13]. Results of $N \geq 110$ ($N \leq 109$) (blue color) are obtained by OD (PD) shapes. Red colors are calculated by OD considering the SC taken from Fig.1. Blue stars for $^{181,183,185}\text{Hg}$ denote the results by the PD obtained w/o SC. The upper contours illustrate the neutron (left half) and proton (right half) prolate shapes of $^{181,183,185}\text{He}$ by their density distributions. The lower contours illustrate oblate shapes of $^{182,184}\text{Hg}$.

Myeong-Hwan Mun, Seonghyun Kim, Myung-Ki Cheoun, W.Y. So, Soonchul Choi et al., Phys. Lett.B 847 (2023) 138298

ANPHA Symposium, Huizhou, Guangdong, China, Nov.

15-16, 2024

3. OE Shape Staggering Results

Potential Energy Curve Evolution with Deform. for **Au**

Nuclear shape transition of Au and no transition in Pb by DRHBc

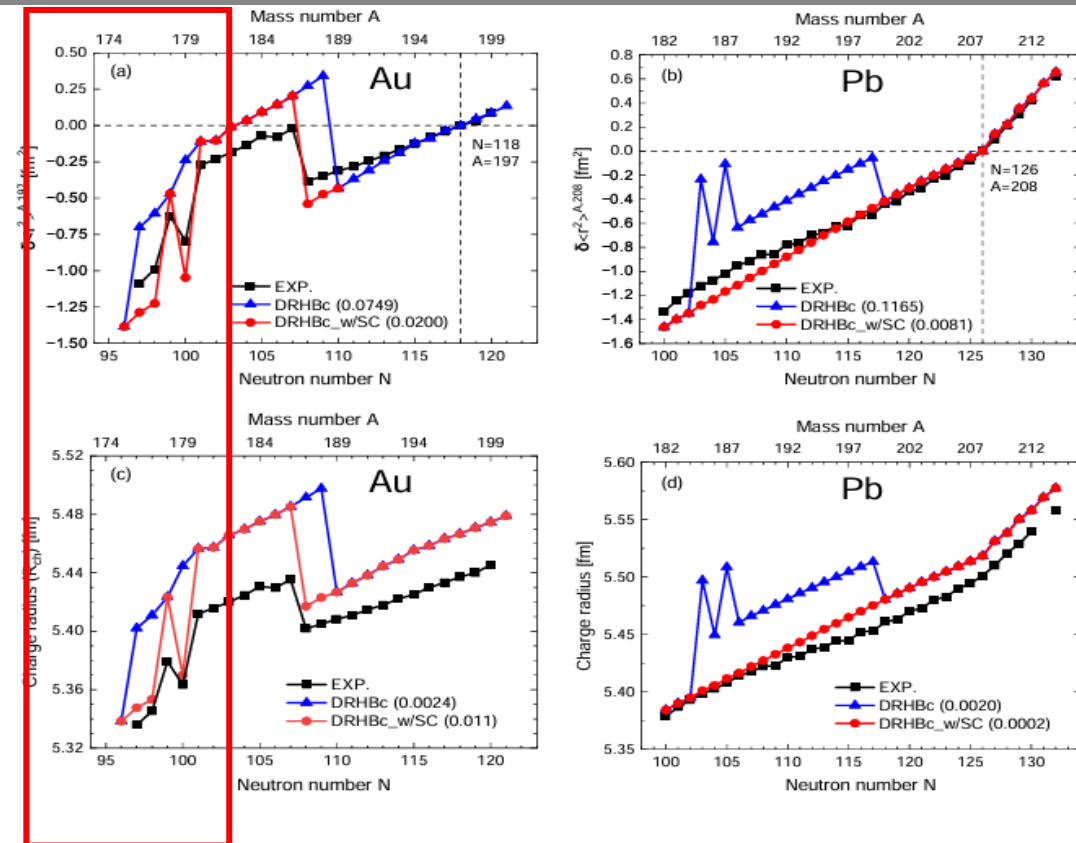
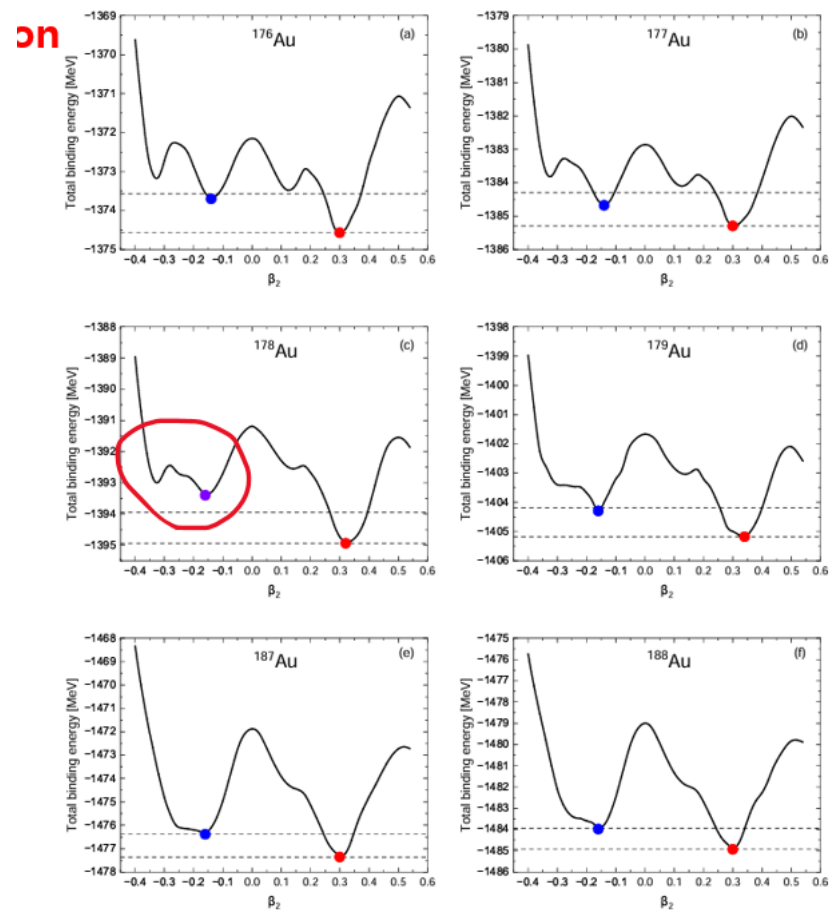


FIG. 7: (Color online) The relative changes of mean square charge radii $\delta\langle r^2 \rangle^{A,197}$ ($\delta\langle r^2 \rangle^{A,208}$) (a) ((c)) and charge radii (c) ((d)) for Au isotopes with $N = 96 \sim 121$ (for Pb isotopes with $N = 100 \sim 132$). For Au, the results denoted in blue triangles are obtained by prolate shapes calculated by the DRHBc theory and red circles in the region are calculated by oblate deformation considering the shape coexistence presented in Fig. 3 and Fig. 4. Considering the shape coexistence, the odd-even shape staggering of charge radii and the abrupt change of charge radii are perspicuously visible for ^{178}Au isotope and provides a reasonable description. For Pb ($100 \leq N \leq 117$), the red data result from the spherical shape coexistence. Black boxes for relative changes of mean square charge radii of Au and Pb are taken from experimental data [7, 35, 110–112, 114]. The numbers in parentheses stand for average rms deviation to the experimental data.

Nuclear shape transition of **Hg isotopes** by Skyrme and Fayans DFTs

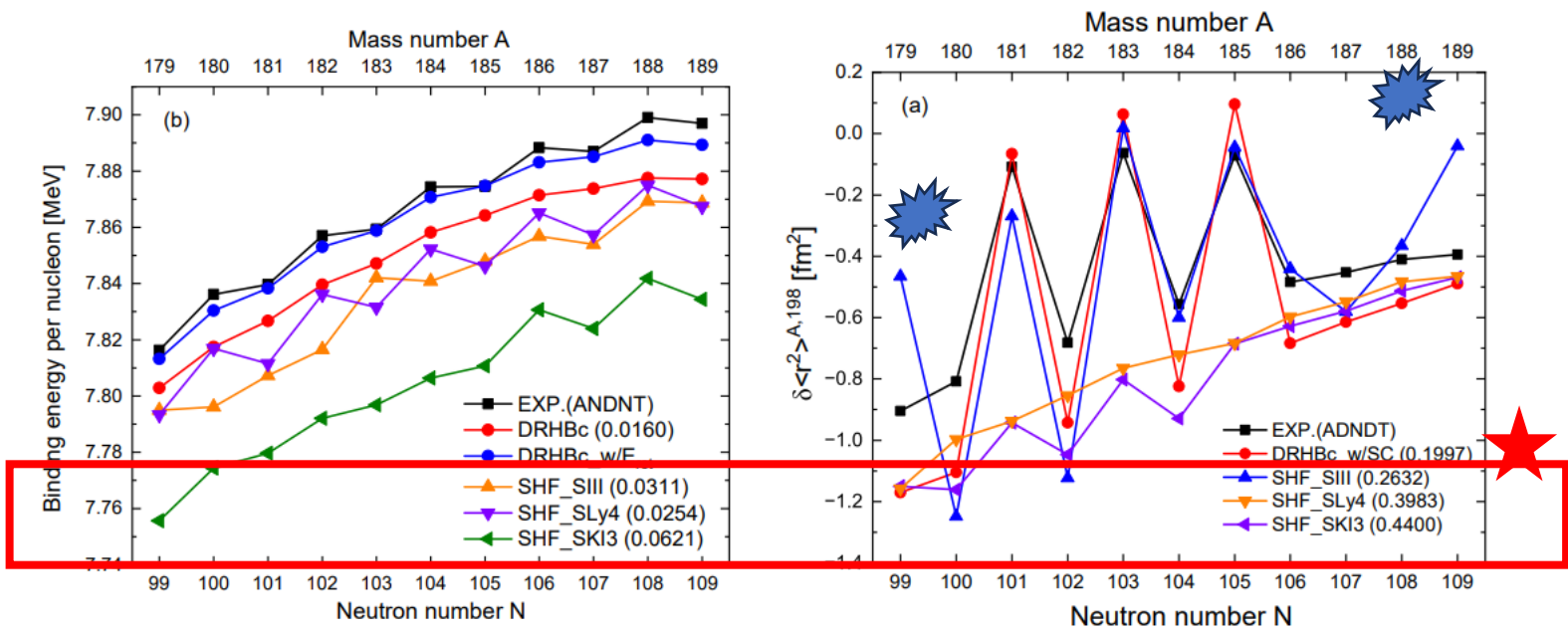


FIG. 4: (Color online) **Comparison of DRHBc and Skyrme models for the BE/A (a) and OES (b). The BE/A (a) corresponds to the Fig.2 (b) and the OES (b) is the same as the Fig. 3 (a). Relative changes of mean square charge radii $\delta \langle r^2 \rangle^{A,198}$ of Hg isotopes. Black boxes stand for the data [13].**

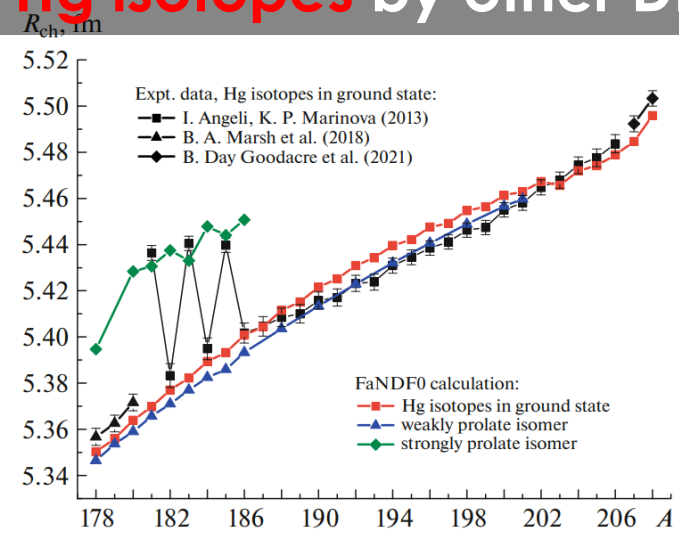


Fig. 6. Charge radii of mercury isotopes.

TABLE I: **Deformations of Hg isotopes used in Fig. 3 and 4 by DRHBc and various parameter sets in Skyrme DFT.**

	DRHBc	SIII [55]	SKI3 [56]	SLy4 [57]	Exp. (β_2 by Q_2)
¹⁷⁹ Hg	-0.1210	0.2751	0.1139	0.1039	—
¹⁸⁰ Hg	-0.1250	0.0000	0.0000	-0.1372	0.1380
¹⁸¹ Hg	0.3458	0.2854	-0.1321	-0.1380	—
¹⁸² Hg	-0.1360	0.0000	0.0000	-0.1437	0.1470
¹⁸³ Hg	0.3367	0.3033	-0.1441	-0.1498	—
¹⁸⁴ Hg	-0.1430	-0.1732	0.0000	-0.1469	0.1560
¹⁸⁵ Hg	0.3118	0.2714	-0.1432	-0.1420	—
¹⁸⁶ Hg	-0.1460	-0.1790	-0.1462	-0.1467	0.1310
¹⁸⁷ Hg	-0.2400	-0.1379	-0.1439	-0.1454	—
¹⁸⁸ Hg	-0.1450	-0.1698	-0.1436	-0.1441	0.1450
¹⁸⁹ Hg	-0.1464	0.2268	-0.1400	-0.1259	—
¹⁹⁸ Hg	-0.1164	-0.1088	-0.1147	-0.1085	0.1064

3. OE Shape Staggering Results

Shape Transition and Occupation Probabilities (Hg)

Red lines for **n1h9/2** shell **decrease** in odd nucleus with the prolate deformation. But **n1i13/2** shell increase with prolate deformation by adding a neutron to e-e Hg.

⇒ like a seasaw from even to odd nuclei !!

For proton, **p1h9/2** shell **increase**, but **p3s1/2** decrease !!

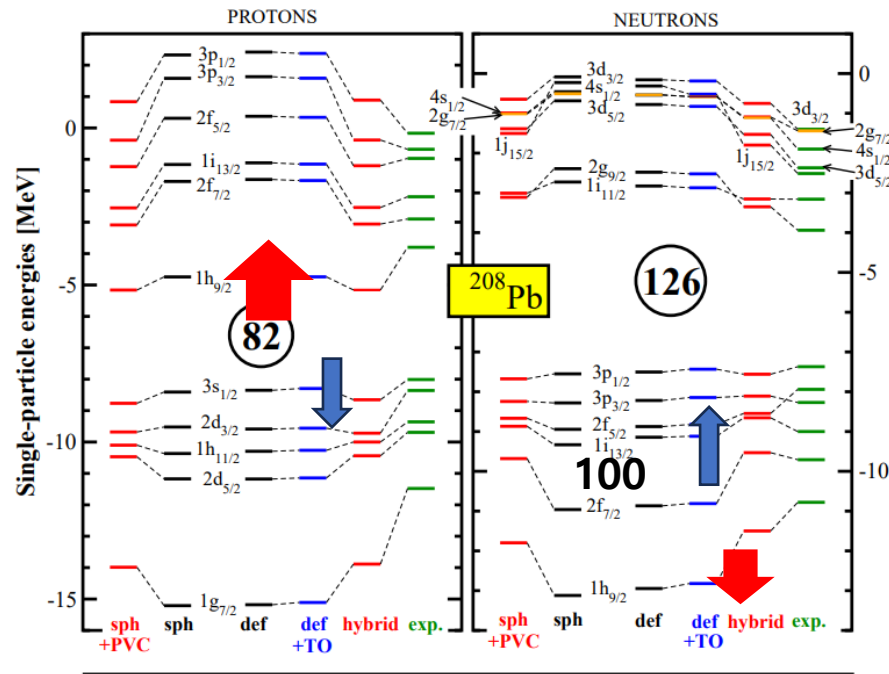


FIG. 5: (Color online) The same as in Fig. 2 but for the spectra of ^{208}Pb . The experimental single-particle levels are based on the data of Refs. [52, 62, 63].

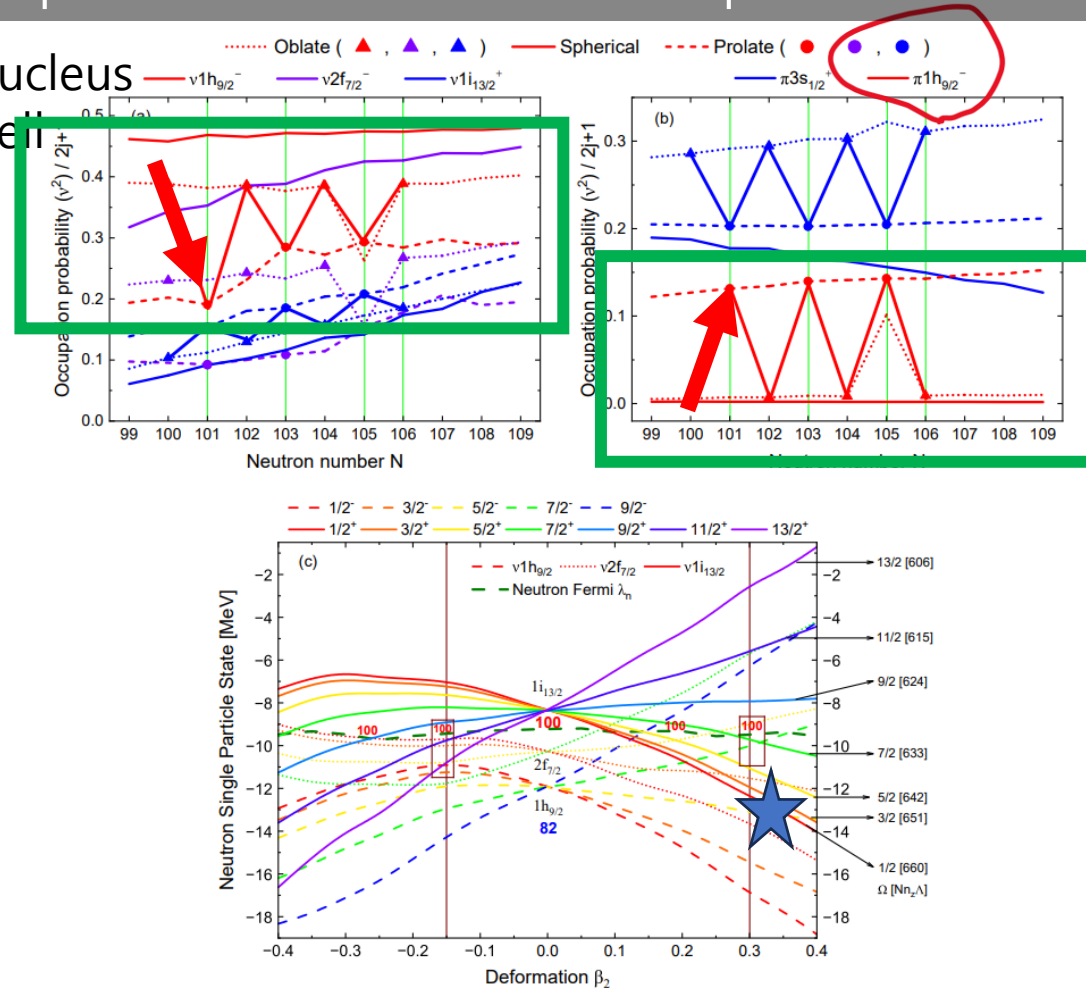


FIG. 4: (Color online) Evolution of OPs of the neutron (a) and proton (b) SPSs for the Hg isotopes. In PD region, the OPs of $\nu 1h_{9/2}$, $\nu 2f_{7/2}$, and $\pi 3s_{1/2}$ states decrease while those of $\nu 1i_{13/2}$ and $\pi 1h_{9/2}$ states increase. This behaviour can be understood by the shell evolution for β_2 with Nilsson quantum numbers $\Omega(N, n_z, \Lambda)$ in the panel (c).

3. OE Shape Staggering Results

Shape Transition of **Au** isotopes

OP of Proton (neutron) $h_{9/2}$ increases (decreases)
, which increases the charge radii !

Similarly to the OES in Hg case

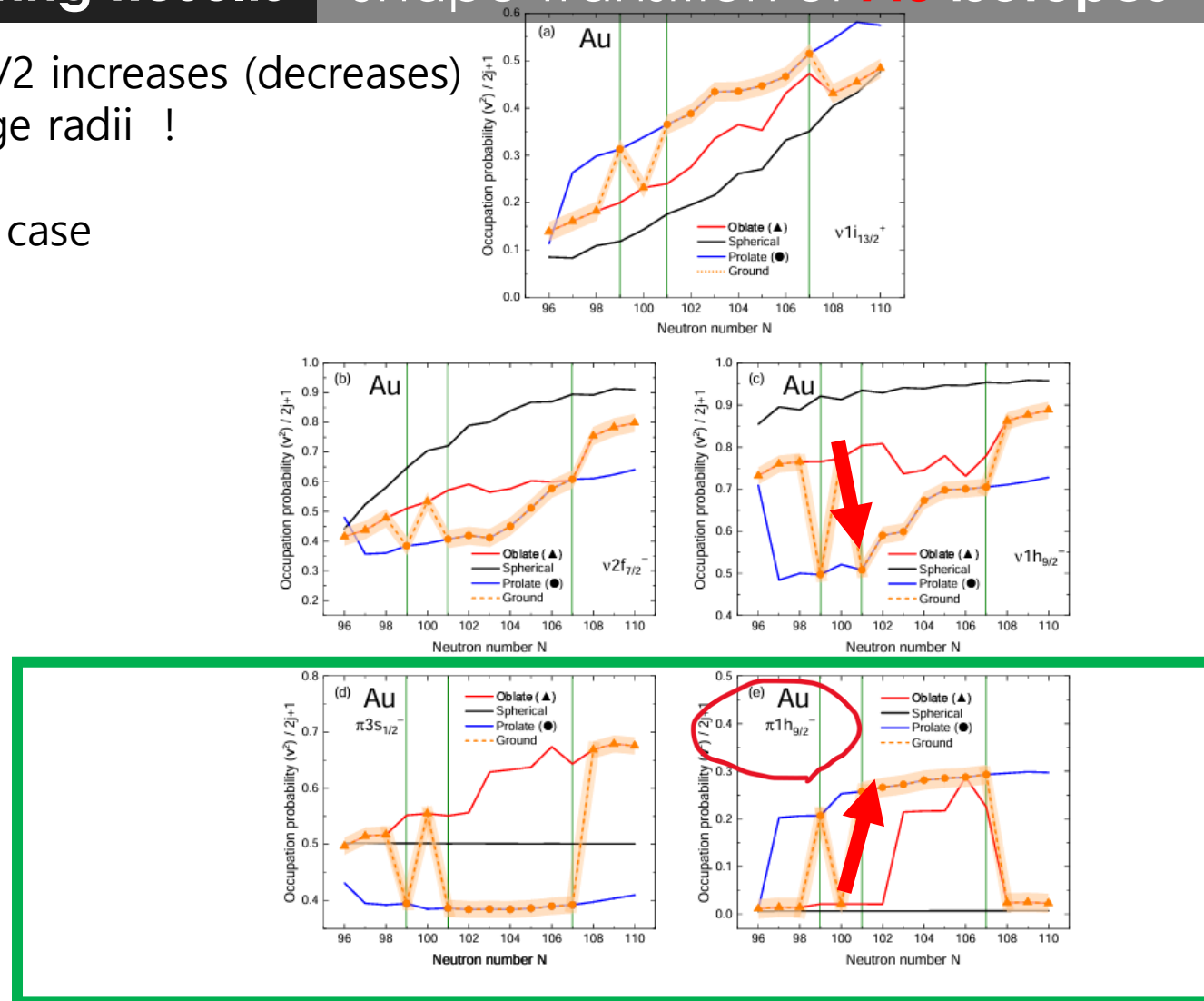
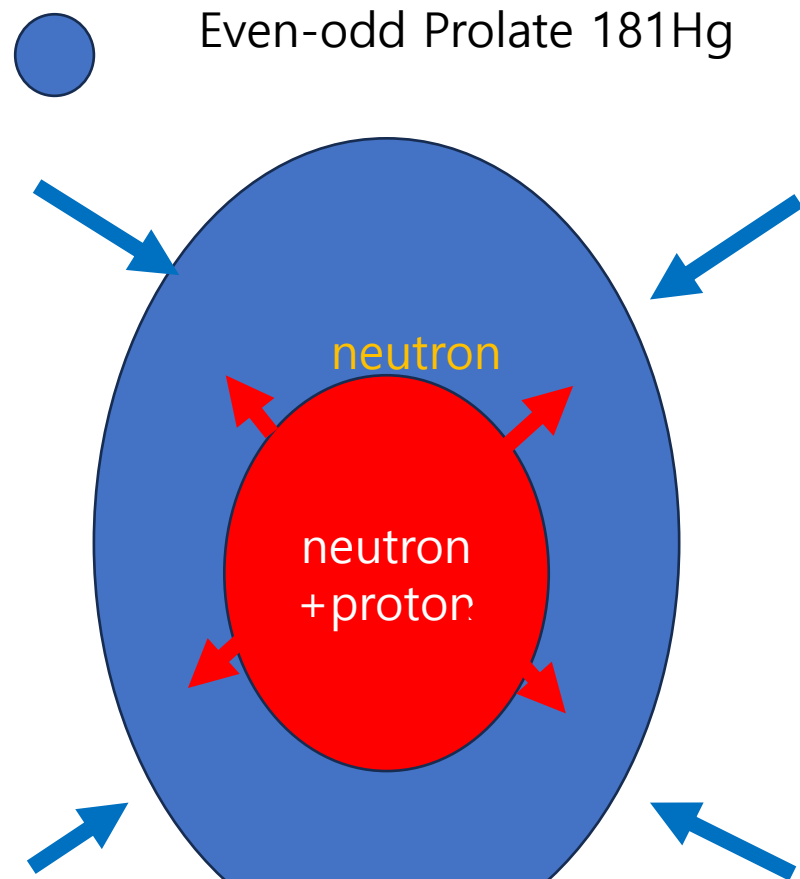


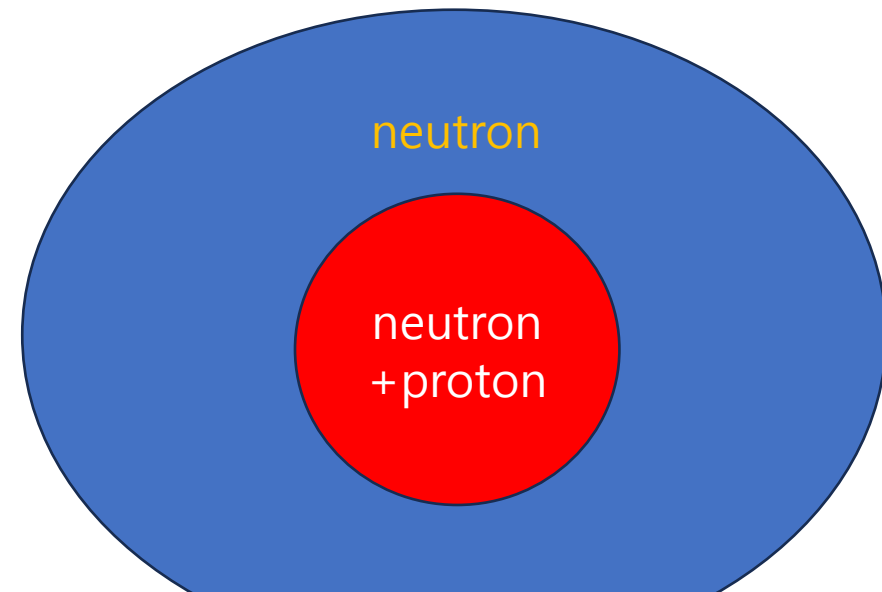
FIG. 8: (Color online) Evolution of occupation probabilities of the neutron $\nu 1i_{13/2}$ (a), $\nu 2f_{7/2}$ (b) and $\nu 1h_{9/2}$ (c) SPSs and proton $\pi 3s_{1/2}$ (d) and $\pi 1h_{9/2}$ (e) SPSs for the Au isotopes. In prolate deformation region, the occupation probabilities of $\nu 1h_{9/2}$, $\nu 2f_{7/2}$, and $\pi 3s_{1/2}$ states decrease while those of $\nu 1i_{13/2}$ and $\pi 1h_{9/2}$ states increase compared to the spherical one. **The shaded regions indicate the ground state considering the shape coexistence.**

3. OE Shape Staggering Results

Why Nuclear Shape Transition in Hg isotopes

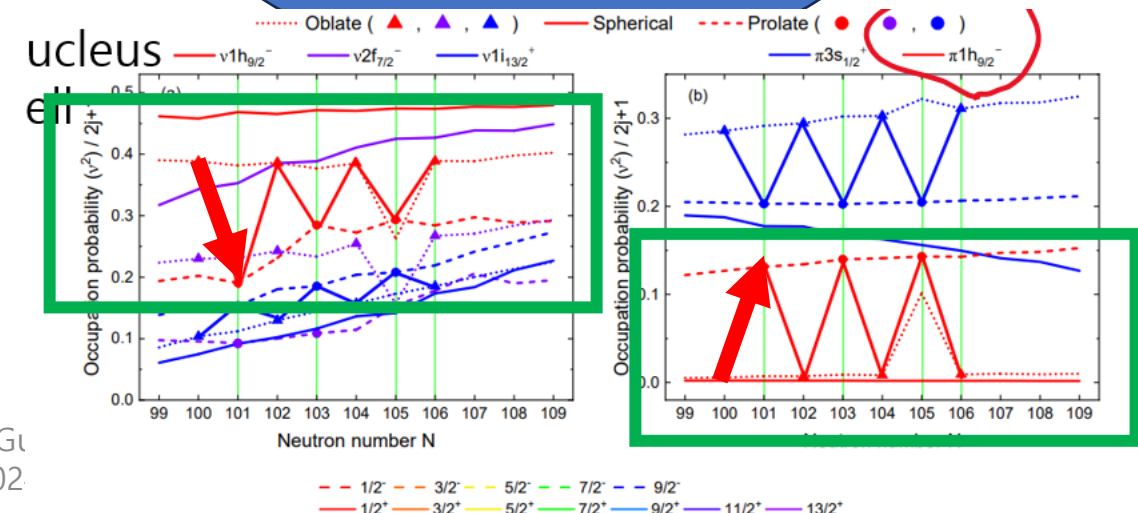


Even-even Oblate 180Hg



Need to know NST evolution !

If we add one neutron to e-e nucleus 180Hg, the OC of $\pi 13/2$ increases and $\nu 1h_{9/2}$ decreases in 181Hg. The increase of charge radii of 181Hg is due to **the increase of $\pi 1h_{9/2}$** shell OC. The OES perhaps come from the tensor interaction ??



3. Kink Structure Results

Kink structure around $N = 126$ shell for Hg isotopes

OC of $1i_{11/2}$ and $2g_{9/2}$ of neutrons increase above $N=126$ shell.
But OC of protons $h_{9/2}$ do not change!

The Kink is to be understood by the swelling of neutrons in the symmetric core, **not by the swelling of protons !!**

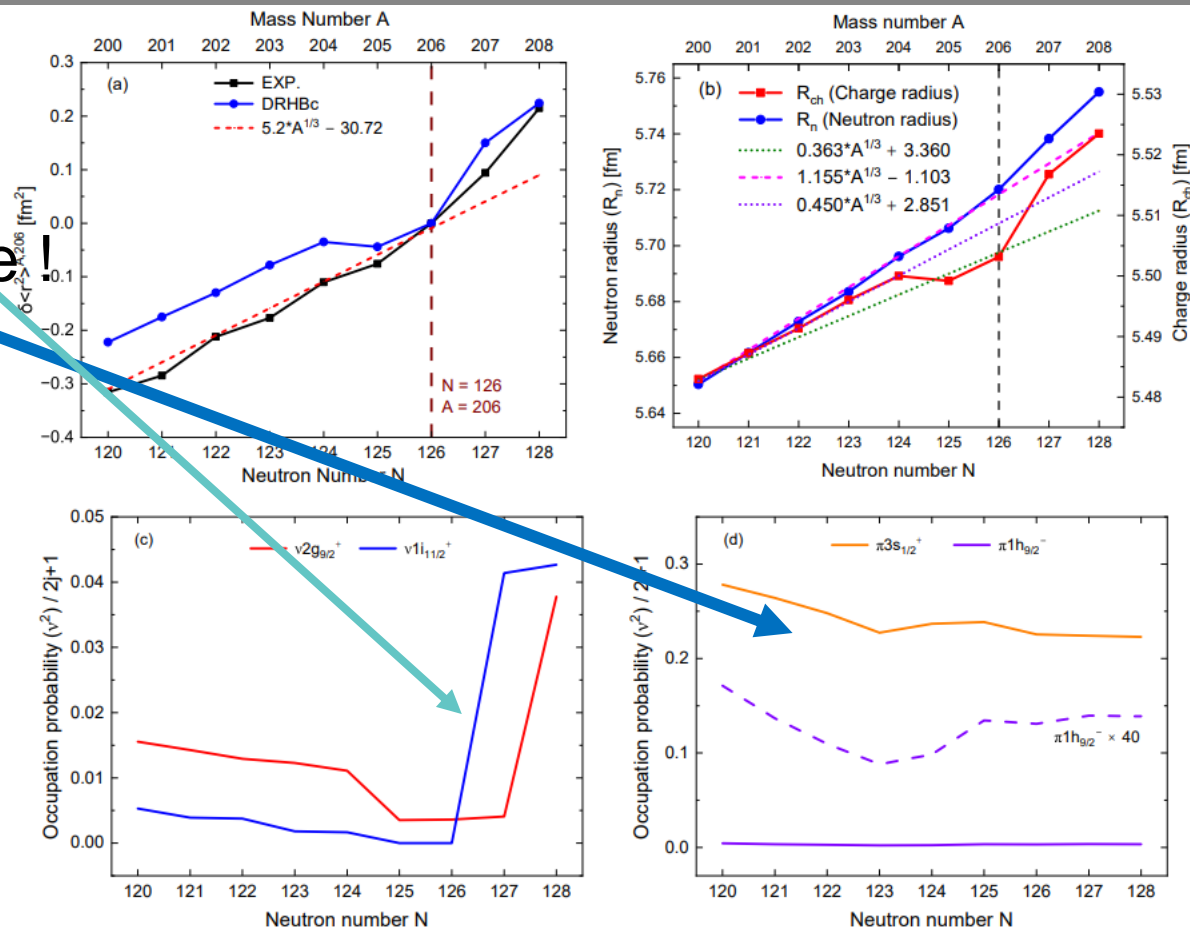
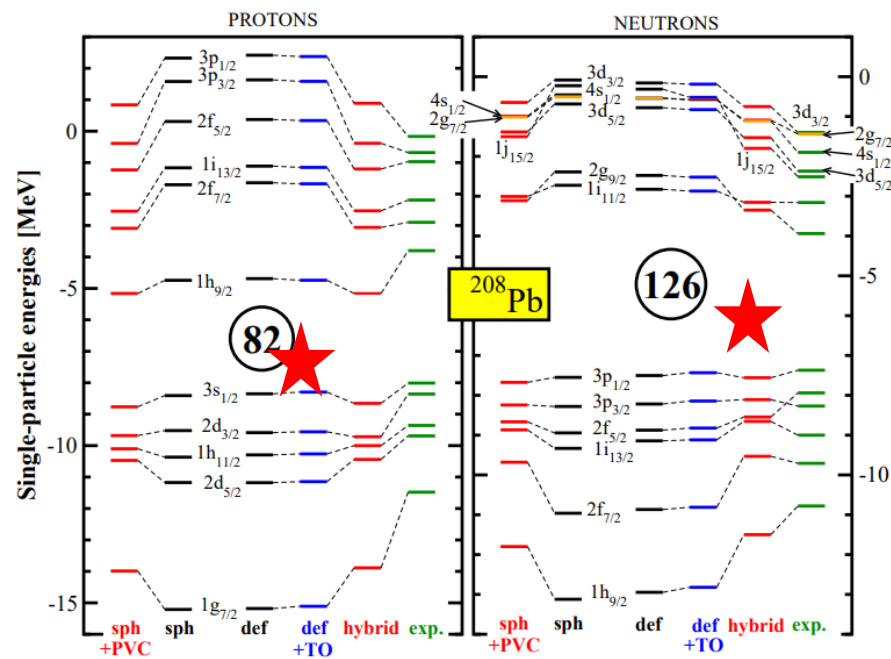


FIG. 5. (Color online) Kink structure in the vicinity of $^{208}\text{Hg}_{126}$ by the relative radius difference (a) and R_n with R_{ch} (b) w.r.t. ^{206}Hg . The dashed lines are just from the continuation of the data before $N = 126$ case to show the kink structure. Panel (c) show the OPs of $\nu 2g_{9/2}$ and $\nu 1i_{11/2}$ state near the magic shell. The larger increase of $\nu 1i_{11/2}$ than $\nu 2g_{9/2}$ state for neutron is evident. OPs of proton states (d) are rarely changed.

3. Kink Structure Results

How to understand the Kink

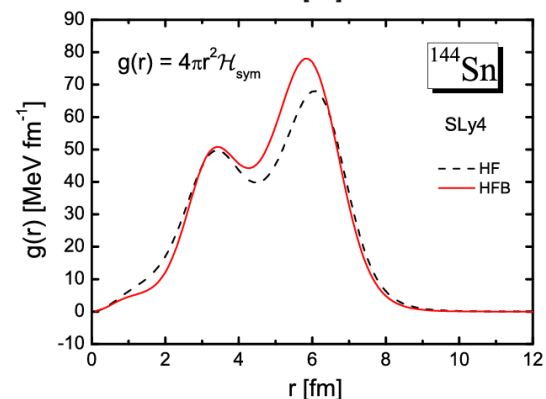
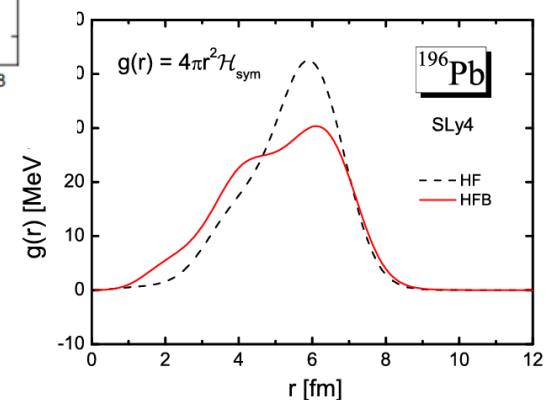
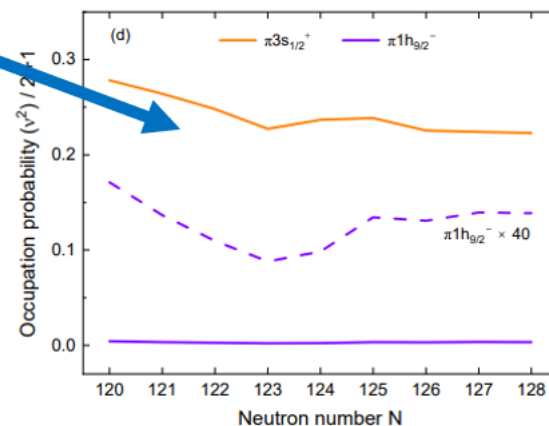
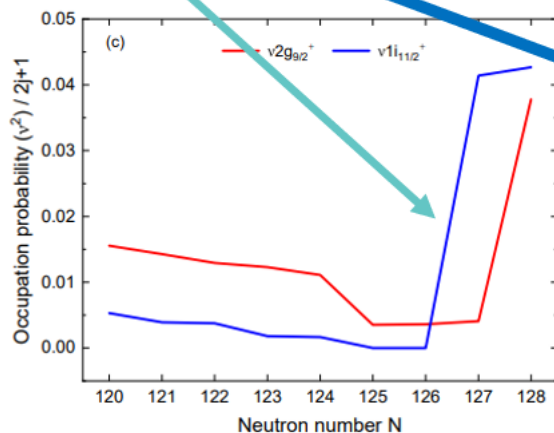
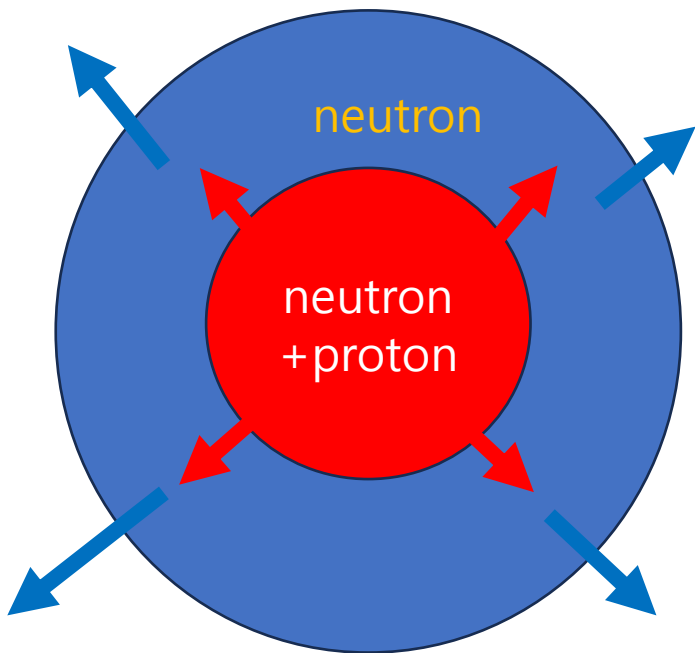


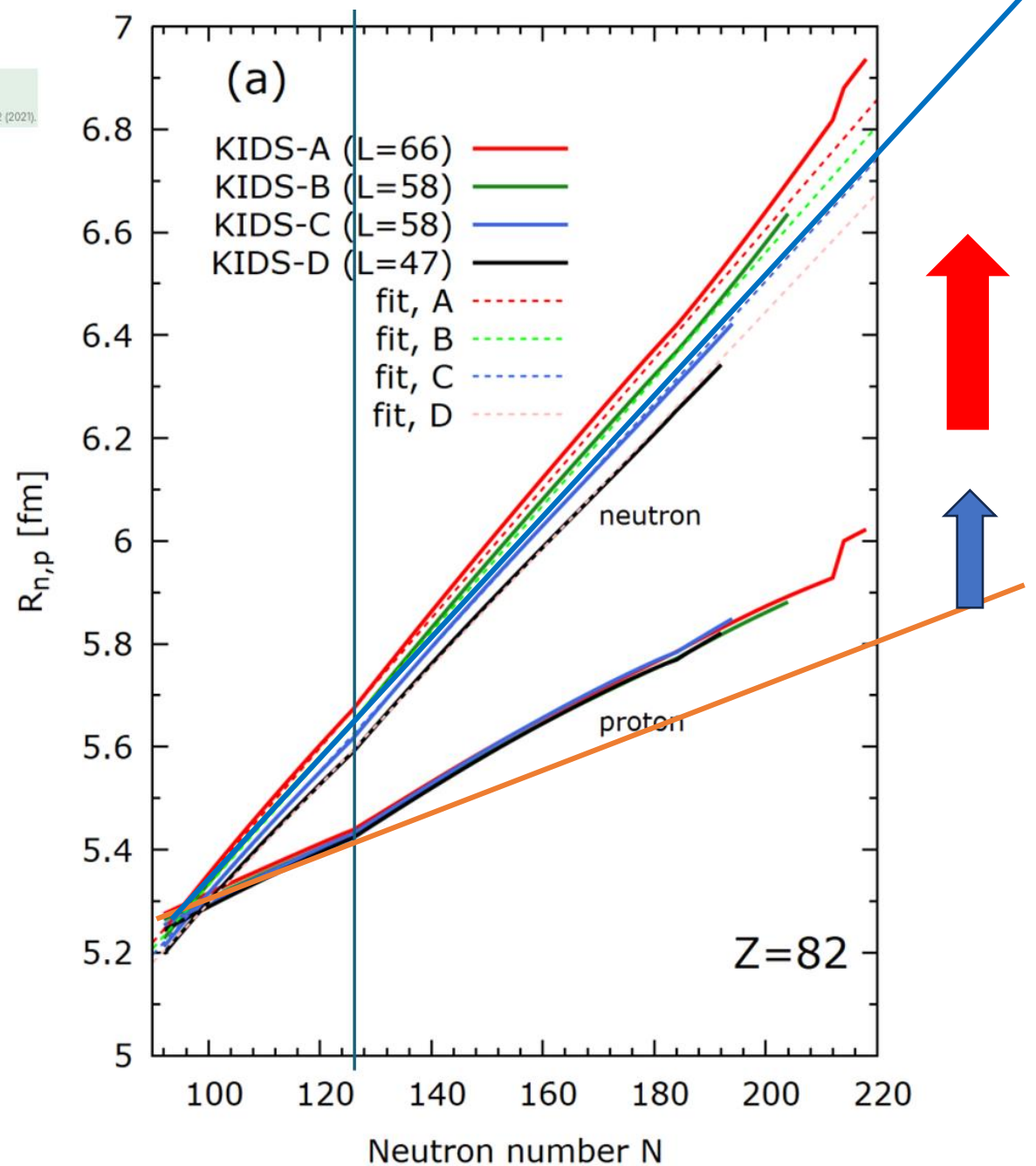
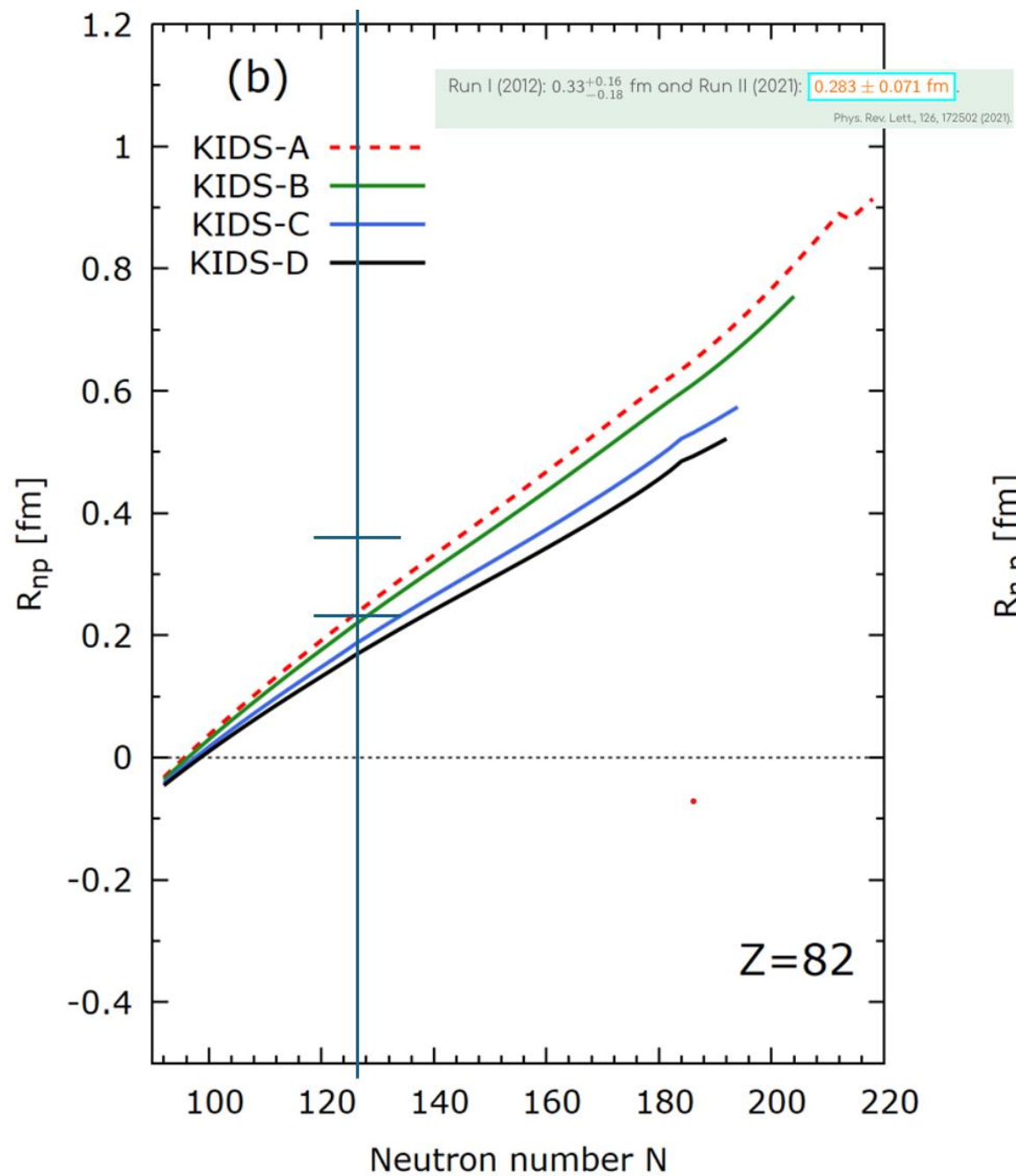
FIG. 4. (Color online) Symmetry energy density distribution $g(r) = 4\pi r^2 \mathcal{H}_{sym}$ in ^{196}Pb (upper panel) and ^{144}Sn (lower panel) obtained by the HF(dashed line) and HFB (solid line) calculation with SLy4 functional.

Phys. Rev. C 96, 024311 (2017)

If we add one neutron to e-e nucleus ^{208}Pb , the OC of **ni11/2** and **n2g9/2** increase ^{209}Pb , but no change of proton OC g9/2 and i11/2.

The increase of charge radii of ^{209}Pb is due to **the increase of neutron side and attract the proton radius.**

The Kink perhaps come from the tensor interaction or symmetry energy ??



Contents

1. Experimental evidences of OES and Kink structures

1-1. Odd-Even (**Shape**) Staggering (OES)

1-2. Kink

2. Deformed Relativistic Hartree Bogoliubov in Continuum (DRHBc) theory and other DFTs

Myeong-Hwan Mun, Seonghyun Kim, Myung-Ki Cheoun, W.Y. So, Soonchul Choi, Phys. Lett.B 847, 138298 (2023)

3. OES and Kink of Hg and Au by DRHBc and other Skyrme DFTs

3-1. OES of Hg and Au

Myeong-Hwan Mun, E. Ha, Y. B. Choi, Myung-Ki Cheoun, PRC 110, 024310 (2024)

3-2. Kink of Hg and Pb



Seonghyun Kim, Myeong-Hwan Mun, Myung-Ki Cheoun and Eunja Ha, PRC 105, 034340 (2022)

4. CM corrections and Magnetic Moments

Y. Tanimura and M. K. Cheoun, PRC 109, 054323 (2024)

5. Summary

Effects of center-of-mass correction and nucleon anomalous magnetic moments on nuclear charge radii

Yusuke Tanimura ^{1,2} and Myung-Ki Cheoun ¹

II. MODEL

A. Relativistic Hartree-Bogoliubov model

We employ an RHB model with DD-ME2 parameter set [50] for the ph channel and Gogny D1S interaction [51,52] for the pp channel. A remark on DD-ME2 is in order: the parameter fit to charge radii was made by $r_{\text{ch}} = \sqrt{\langle r^2 \rangle_p + (0.8 \text{ fm})^2}$, where $\langle r^2 \rangle_p$ is the mean-squared (MS) radius of point-proton density distribution, and $(0.8 \text{ fm})^2$ is a correction for the charge radius of the proton itself, with BCS calculations instead of Hartree-Bogoliubov. The CM correction and anomalous magnetic coupling described in the following subsections were not considered. See Refs. [50,53–59] for details of the RHB model and the DD-ME2 parameter set. We impose the spherical symmetry and solve the RHB equations in the radial coordinate space.

Contribution of nucleon anomalous magnetic moment to charge density

EM current density operator

$$\hat{j}_{\text{em}}^\mu(p', p) = \bar{\psi}(p') \left[F_1(Q^2) \gamma^\mu + F_2(Q^2) \frac{i\hbar}{2mc} Q_\nu \sigma^{\mu\nu} \right] \psi(p)$$

$$F_1(Q^2) = F_1(0) = q, F_2(Q^2) = F_2(0) = \kappa$$

$$j_{\text{em}}^\mu(x) = q \bar{\psi}(x) \gamma^\mu \psi(x) + \frac{\kappa \hbar}{2mc} \partial_\nu \bar{\psi}(x) \sigma^{\mu\nu} \psi(x),$$

Mean-field approximation

$$\rho_{\text{ch}} \equiv \langle j_{\text{em}}^0 \rangle = \sum_\alpha v_\alpha^2 q_\alpha \psi_\alpha^\dagger \psi_\alpha + \sum_\alpha v_\alpha^2 \kappa_\alpha \frac{\hbar}{2mc} \nabla \cdot (\bar{\psi}_\alpha i \alpha \psi_\alpha) = \rho_p + \rho_\kappa$$

Mean-square charge radius

$$\begin{aligned} \langle r^2 \rangle_{\text{ch}} &= \frac{1}{Z} \int d^3r r^2 [\rho_p(\mathbf{r}) + \rho_\kappa(\mathbf{r})] + \langle r_p^2 \rangle + \frac{N}{Z} \langle r_n^2 \rangle \\ &= \langle r^2 \rangle_p + \langle r^2 \rangle_\kappa + \langle r_p^2 \rangle + \frac{N}{Z} \langle r_n^2 \rangle \end{aligned}$$

$Q = p' - p$ (電磁場の運動量)

$$F_1(0) = q$$

$$2[F_1(0) + F_2(0)] = g = 2(q + \kappa)$$

$q = 1, \kappa = 1.793$ for p

$q = 0, \kappa = -1.913$ for n

ψ_α : single-particle wfn

v_α^2 : occupation probability

Finite size of nucleon

$$\langle r_p^2 \rangle = 0.8409(4)^2 \text{ fm}^2$$

$$\langle r_n^2 \rangle = -0.1155(17) \text{ fm}^2$$

<https://pdglive.lbl.gov/>

4. More Corrections

CM corrections and AMM effects on Chare Radius

Neutron
squared radius

$$\begin{aligned}
 N \langle r^2 \rangle_{n,corr} &= \left\langle \sum_{i \in n} (\mathbf{r}_i - \mathbf{R}_G)^2 \right\rangle \\
 &= \left\langle \sum_{i \in n} r_i^2 \right\rangle - \frac{1}{A} \left[\left\langle \left(\sum_{i \in n} \mathbf{r}_i \right)^2 \right\rangle - \left\langle \left(\sum_{i \in p} \mathbf{r}_i \right)^2 \right\rangle \right] - \frac{Z}{A^2} \left\langle \left(\sum_{i=1}^A \mathbf{r}_i \right)^2 \right\rangle \\
 &\equiv N \left[\langle r^2 \rangle_n + \Delta_n^{(CM1)} + \Delta_n^{(CM2)} \right]
 \end{aligned}$$

1- and 2-body parts of the CM correction:

$$\Delta_n^{(CM1)} = -\frac{2}{A} \langle r^2 \rangle_n + \frac{1}{A} \langle r^2 \rangle_m$$

TM1 & TM2, Sugahara and Toki, NPA**579**, 557 (1994).
PK1 & PKDD, Long et al., PRC**69**, 034319 (2004).

$$\begin{aligned}
 \Delta_n^{(CM2)} &= + \frac{1}{NA} \left[\sum_{\alpha\beta \in n} (v_\alpha^2 v_\beta^2 - u_\alpha v_\alpha u_\beta v_\beta) |\langle \alpha | \mathbf{r} | \beta \rangle|^2 - \sum_{\alpha\beta \in p} (v_\alpha^2 v_\beta^2 - u_\alpha v_\alpha u_\beta v_\beta) |\langle \alpha | \mathbf{r} | \beta \rangle|^2 \right] \\
 &\quad + \frac{Z}{N} \Delta_m^{(CM2)}
 \end{aligned}$$

Note that $A\Delta_m^{(CMi)} = N\Delta_n^{(CMi)} + Z\Delta^{(CMi)}$.

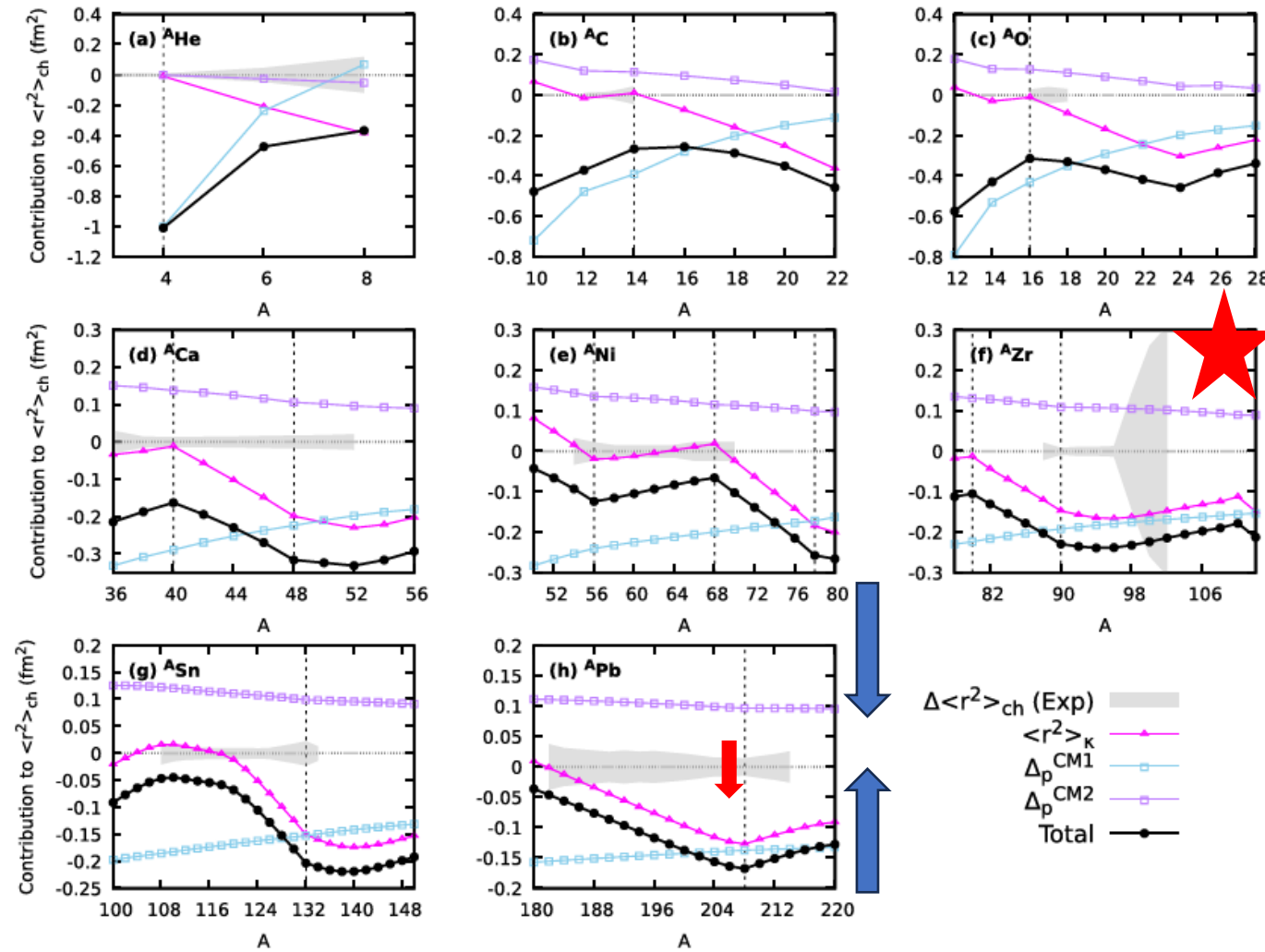


FIG. 1. Contributions of each correction term to the MS charge radius for (a) He, (b) C, (c) O, (d) Ca, (e) Ni, (f) Zr, (g) Sn, and (h) Pb isotopes. Magenta triangles, the anomalous magnetic contribution $\langle r^2 \rangle_{\kappa}$; sky-blue and purple squares, the one- and two-body CM corrections, $\Delta_p^{(\text{CM1})}$ and $\Delta_p^{(\text{CM2})}$, respectively; black dots, the total correction $\langle r^2 \rangle_{\kappa} + \Delta_p^{(\text{CM1})} + \Delta_p^{(\text{CM2})}$. The gray bands show the size of experimental uncertainty $\Delta \langle r^2 \rangle_{\text{ch}} \in [(r_{\text{ch}} - \delta r_{\text{ch}})^2 - r_{\text{ch}}^2, (r_{\text{ch}} + \delta r_{\text{ch}})^2 - r_{\text{ch}}^2]$, with r_{ch} and δr_{ch} being the measured value of the charge radius and the associated error, respectively. The data for $^{54,56}\text{Ni}$ are taken from Ref. [3], data for $^{58-70}\text{Ni}$ are taken from Ref. [4], and data for the others are taken from Refs. [1,2]. The vertical lines are drawn at $N = 2, 8, 20, 28, 40, 50, 82$, and 126 .

We also mention here the connection of our approach to the approximate projection method [33] via harmonic-oscillator approximation. Within the harmonic-oscillator model as described in Appendix B, the total CM correction given by Eqs. (2)–(5) satisfies

$$\Delta_p^{(\text{CM1})} + \Delta_p^{(\text{CM2})} = -\frac{9\hbar^2}{4\langle P_{\text{CM}}^2 \rangle}, \quad (21)$$

where P_{CM} is the CM momentum. On the other hand, it was shown in Ref. [33] that the second-order Gaussian-overlap approximation to the momentum projection yields an effect identical to that with a harmonic-oscillator approximation. In their approximation, the nuclear charge form factor is corrected by an additional factor of $\tilde{\rho}_{\text{CM}}(\mathbf{q}) = \exp(\frac{3\hbar^2 \mathbf{q}^2}{8\langle P_{\text{CM}}^2 \rangle})$ [33,42]. The additional factor on the charge form factor, $\tilde{\rho}_{\text{ch}}(\mathbf{q}) \rightarrow \tilde{\rho}_{\text{ch}}(\mathbf{q})\tilde{\rho}_{\text{CM}}(\mathbf{q})$, yields an additional term $-6\frac{d\tilde{\rho}_{\text{CM}}(0)}{dq^2} = -\frac{9\hbar^2}{4\langle P_{\text{CM}}^2 \rangle}$ in the MS charge radius, which coincides with the total CM correction in Eq. (21). Thus our approach yields, for heavy nuclei, approximately the same correction as the projection method, but not for light or weakly

Summary and Conclusion

1. Our findings highlight the significance of SC in understanding **the OES observed in the Hg isotopes**.
2. Taking into account OD for most Hg isotopes, except for **181,183,185Hg**, by **the shape coexistence** is crucial for explaining the OES phenomenon.
3. But these three (**prolate-shaped**) odd nuclei are excluded from the SC and exhibit larger charge radii.
4. It may indicate that the OES can serve as a useful tool for identifying the SC in Hg isotopes, or vice versa.
5. **The nuclear shape transition and the evolution of OP by the additional neutron** in the range of 180-186Hg isotopes is essential for understanding the prominent OES observed in the Hg isotopes. **The OES of Au has been calculated by DRHBc and reproduce the OES data.**
6. Furthermore, the DFT models like DRHBc model successfully reproduces **the kink structure** observed around th
7. This kink structure arises from **the increase in the OPs of $i_{11/2}$ and $2g_{9/2}$ states** beyond the magic shell, influenced by the multi-particle and multi-hole interactions.
8. **This swelling effect of symmetric core** pushes the proton states to the outer nuclear surface by the symmetry energy residing on the symmetric core surface and **perhaps to the tensor force.**
9. The second order CM correction may cancel the 1st order CM correction, so that the SO effect from ANM moment becomes meaningful.
10. It would be interesting to further investigate the OES and the kink structures of charge radii and matter radii in Ca, K, and Pb isotopes **in the vicinity of each magic shell** using the DFT models in future studies.

Remarks and Conclusion

1. Other corrections, such as **CM correction and ANM contribution** are also the remained quantities in the charge radii study.
2. **Charge symmetry breaking** is another interesting topic which affects the charge radii and/or the density distribution in nuclei.
3. Matter effects, such as effective masses, **symmetry energy and equation of state**, are to be discussed in detail in the future.
4. Along this line, the study of **NST in the experiment (LEES)** could give valuable information for charge radii study of unstable nuclei.
5. Laser spectroscopy for the isotope shift from the hyperfine interaction and LEE scattering could complement the charge radii and density distribution (**proton as well as neutron density**) study.
(Xiaofei Yang Talk)
6. Specifically, **the OES of Ca and Zr is to be studied in both experimental and theoretical fields.**



Thanks for
your attention !!

 **SOMEG**
Origin of Matter and Evolution of Galaxies
우주 물질 중점연구소